The Meteoritical Society

Meteoritics & Planetary Science 59, Nr 9, 2545–2564 (2024)
doi: 10.1111/maps.14235

Mineralogy of the Martian mantle inferred from bulk chemical compositions

Shuying YANG [1], Munir HUMAYUN [1]*, and Kevin RIGHTER [2,3]

[1]National High Magnetic Field Laboratory and Department of Earth, Ocean & Atmospheric Science, Florida State University, Tallahassee, Florida, USA
[2]Astromaterials Research and Exploration Sciences, NASA Johnson Space Center, Houston, Texas, USA
[3]Department of Earth and Environmental Sciences, University of Rochester, Rochester, New York, USA

***Correspondence**
Munir Humayun, National High Magnetic Field Laboratory and Department of Earth, Ocean & Atmospheric Science, Florida State University, Tallahassee, FL 32310, USA.
Email: humayun@magnet.fsu.edu

(Received 07 April 2022; revision accepted 19 June 2024)

Abstract–Understanding the mineralogy of the Martian mantle is essential for constructing geochemical and geophysical models of Mars. This study employs the pMELTS program to determine the mineralogy at the solidus from 11 published bulk silicate Mars (BSM) compositions, within a pressure range of 2–5 GPa. The pMELTS results align with experimental data and calculations from another thermodynamic program (Perple_X/stx11). Mineral modes from compositional models based on Martian meteorite geochemistry show relatively consistent abundances modes (olivine: 48–56 wt%, orthopyroxene: 20–25 wt%, clinopyroxene: 15–17 wt%, garnet: 6–9 wt%). In contrast, mineral modes from compositional models that are not based on Martian meteorite geochemistry exhibit a wider range of olivine and garnet abundances. Additionally, we constrained the mineral modes of the Martian mantle using trace element partitioning and partial melting models. Our calculations indicate that melts derived from mantle sources with a hypothesized garnet content of 5–10 wt% closely match the analyzed compositions of shergottites, validating the garnet mode (6–9 wt%) constrained in our pMELTS calculations. Extracting low-degree (<4 wt%) melts from a BSM to form depleted Martian mantle (DMM) does not significantly alter the mineralogical modes of solid residues, but it does lead to substantial trace elemental depletion in the DMM. Therefore, enriched, intermediate, and depleted shergottite sources are likely characterized by similar mineral modes yet differ in incompatible element abundances.

INTRODUCTION

The mineralogy of a planet's mantle determines the type of the volcanism that plays an important role in the composition of the surface environment, including crust, atmosphere, hydrosphere, and biosphere. On Earth, mantle xenoliths and peridotite outcrops provide essential clues to the broader nature of the mantle (Jagoutz et al., 1979; Pearson et al., 2003; Sobolev et al., 2005). The mineralogical composition of Mars' mantle is not known from direct samples. There are few sources of information to constrain the mineralogy: estimates of the bulk chemical composition of Mars, analyzing the mineral compositions of phenocrysts and xenocrysts in primitive basalts, bulk compositions of Martian meteorites, compositions of surface rocks from in situ rover measurements, and geophysical constraints on the density of the Martian interior.

Mars is often regarded as a failed planet that accreted early in solar system history (Jacobson & Walsh, 2015; Morbidelli et al., 2012). The differentiation of bulk silicate Mars (BSM) may follow either of two distinct paths: low-degree melting of BSM resulting in the formation of a primitive crust and a residual depleted mantle material (DMM), or high-degree melting resulting in a Mars Magma Ocean (MMO) that crystallizes to a stratified

cumulate where the residual liquid forms the primitive Martian crust. In both scenarios, later volcanism taps reservoirs in the differentiated mantle that may include DMM. As an embryonic planet, Mars clearly reached temperatures high enough during accretion for core–mantle–crust differentiation but need not have gone through an MMO stage (Barnes et al., 2020). Many workers have considered an MMO stage on early Mars to have occurred to explain the chronology of mantle differentiation inferred from extinct radionuclides (Debaille et al., 2008), mantle composition (Borg & Draper, 2003), and core formation (Righter et al., 2015). The initial composition of the BSM could have undergone mineralogical differentiation, resulting in distinct cumulate mantle domains. The specific characteristics of these domains would depend on the mineralogical mode of the original cumulate pile and subsequent cumulate overturn and convective mixing (Elkins-Tanton, 2008).

Non-clastic Martian meteorites are classified into three main types based on their mineralogical and isotopic characteristics: shergottites, nakhlites, and chassignites, from which geochemical evidence supporting a differentiated Martian mantle is obtained. Shergottites largely fall into three major compositional groups: enriched, intermediate, and depleted, the mantle sources of which were established early in Martian history (Debaille et al., 2008; Foley et al., 2005; Righter et al., 2020; Udry et al., 2020). There is substantial debate about whether these three groups represent three distinct mantle source regions created in the post-magma ocean stage (Bouvier et al., 2018; Brandon et al., 2000, 2012; Collinet et al., 2023; Debaille et al., 2008; Ferdous et al., 2017; Kruijer et al., 2020; Lapen et al., 2010) or a single, depleted mantle source region that variably assimilated an ancient Martian crustal component (Agee et al., 2013; Day et al., 2018; Humayun et al., 2013; Norman, 1999; Peters et al., 2015; Wu et al., 2021). At a minimum there must be BSM and DMM on Mars, and possibly up to four mantle sources (primitive, enriched, intermediate, and depleted), although there could be many more (e.g., Udry et al., 2020). Because the enriched and intermediate mantle sources are likely to be transitional types between BSM and DMM, this study will focus on these two endmembers. This is not intended to exclude the possibility of there being other mantle endmembers. This manuscript utilizes the acronym DMM to refer specifically to the depleted Martian mantle, as discriminated from the more commonly used acronym DMM that designates the terrestrial depleted MORB (mid-ocean ridge basalt) mantle.

Chemical models of BSM follow several key premises: cosmochemical groups are based either on elemental (Morgan & Anders, 1979; Taylor, 2013; Wänke & Dreibus, 1994; Yoshizaki & McDonough, 2020) or oxygen isotopic variations (Lodders & Fegley, 1997; Sanloup et al., 1999) in chondrites and Martian meteorites; geophysical models are based on density and moment of inertia (Khan et al., 2018; Khan & Connolly, 2008; Ohtani & Kamaya, 1992).

Key parameters that need to be constrained in any chemical model of mineralogy of the mantle include the relative abundances of Al, Ca, and Ti in a Mg-silicate mantle, the Mg/Fe ratio, the Fe/Mn ratio, and the abundances of alkalis and phosphorus. Some of these parameters are best determined from meteorite data, including the Mg/Fe and Fe/Mn ratios (Taylor, 2013; Wänke & Dreibus, 1994; Yoshizaki & McDonough, 2020).

Several attempts were made to constrain the mantle mineralogy of BSM and DMM. Bertka and Fei (1997) performed high-pressure multianvil experiments (2–23.5 GPa) with a composition of BSM from Dreibus and Wänke (1985) to determine the mineralogy of the Martian interior. Yoshizaki and McDonough (2020) used the thermodynamic parameters of Stixrude and Lithgow-Bertelloni (2011) in Perple_X computer program (Connolly, 2009) to calculate the mineralogy for their estimated BSM composition. Borg and Draper (2003) calculated mineral modes of DMM using a two-step approach. The first step calculated the crystallization sequence for the Martian magma ocean (MMO) and the second step confirmed that the trace elemental composition in the partial melts derived from this DMM composition is consistent with that of the depleted shergottite (e.g., QUE 94201) source. Debaille et al. (2008) constrained the source mineralogy of DMM using their ^{176}Lu-^{176}Hf and ^{147}Sm-^{143}Nd systematics. Yet, neither the compositional effect on the mantle mineralogy of Mars nor the mineralogical relationship between BSM and DMM has been pursued in previous studies.

Our knowledge of the mineralogical properties of planetary mantles is based on experimental studies of mantle partial melting at various *P*–*T* conditions. In this study, the mineralogy of the Martian mantle is constrained by using the pMELTS calibration (Asimow & Ghiorso, 1998; Ghiorso et al., 2002) to model the subsolidus mineralogy of the various compositional estimates of the BSM (Khan & Connolly, 2008; Lodders & Fegley, 1997; Morgan & Anders, 1979; Ohtani & Kamaya, 1992; Sanloup et al., 1999; Taylor, 2013; Wänke & Dreibus, 1994; Yoshizaki & McDonough, 2020). Phase compositions from experimental studies of the melting of putative Martian mantle compositions (Bertka & Fei, 1997; Ding et al., 2020; Matsukage et al., 2013) are used to validate the pMELTS output and to assess the effect of partial melting degree on the mineralogy of melting residues. Data from phenocryst/xenocryst assemblages in Martian meteorites are used to determine important parameters, such as Mg# (Aoudjehane et al., 2012; Balta et al., 2015), which compositional models rely on. The pMELTS modeled

mineralogy of BSM is used to derive a composition for the DMM. The incompatible element compositions of partial melts of DMM are then compared to the partitioning behavior of trace elements in Martian basalts to constrain the mineralogical modes of shergottite sources.

METHODOLOGY

MELTS Model Version Selected

To calculate the phase equilibria of a given starting composition, MELTS uses Gibbs free energy minimization to find the most stable set of phases that can coexist under the given conditions. MELTS has proven to be a useful tool in modeling various magmatic processes on Mars (e.g., Balta & McSween, 2013; Elkins-Tanton et al., 2005; Udry et al., 2018). Some studies have argued that MELTS is less accurate in predicting the composition of partial melts derived from the Martian mantle because of the higher FeO content of the latter (Collinet et al., 2015, 2021). The Martian mantle has an average FeO content (14–18 wt%) that is higher than that of the terrestrial mantle, for example, KLB-1 (8 wt%; Davis et al., 2011; McDonough & Sun, 1995). Thus, applying MELTS to Mars requires incorporating the results of melting experiments conducted with Martian mantle compositions. Only one experimental study of Martian compositions (Longhi et al., 1992) was included in the original calibration database of MELTS (Ghiorso & Sack, 1995) and pMELTS (Ghiorso et al., 2002).

Since the publication of MELTS, many experimental studies have been performed on model compositions of Mars (e.g., DW94 and LF97) to investigate the melting process of a Martian mantle composition under varying P–T conditions (Agee & Draper, 2004; Bertka & Fei, 1997; Bertka & Holloway, 1994a, 1994b; Collinet et al., 2015, 2021; Ding et al., 2020; Duncan et al., 2018; Matsukage et al., 2013). A database of these melting experiments was used to calibrate a new model called MAGMARS to calculate the composition of Martian primary melts and to investigate thermodynamic properties of the Martian mantle (Collinet et al., 2021). But so far, MAGMARS does not support the function that performs the calculation of heterogeneous phase equilibria in the near-solidus region.

In this study, we used the AlphaMELTS 1.9 (Smith & Asimow, 2005) front end for the program and the pMELTS calibration (Asimow & Ghiorso, 1998; Ghiorso et al., 2002; Ghiorso & Sack, 1995) to calculate subsolidus phase relations of the Martian mantle. We opted to use pMELTS over MELTS due to its suitability for modeling processes at high pressure, whereas MELTS is designed primarily for magmatic phase relations at low pressure. The calculated results from pMELTS in this study are directly compared with the experimental findings (where applicable) using an identical initial composition. The starting compositions, temperature, pressure, oxygen fugacity (T, P, fO_2), and conditions adopted for the calculation are listed below and presented in Table 1.

Starting Compositions

Eight compositional models of BSM (Khan & Connolly, 2008; Lodders & Fegley, 1997; Morgan & Anders, 1979; Ohtani & Kamaya, 1992; Sanloup et al., 1999; Taylor, 2013; Wänke & Dreibus, 1994; Yoshizaki & McDonough, 2020) and the synthetic starting compositions used in three experimental studies (Agee & Draper, 2004; Bertka & Fei, 1997; Matsukage et al., 2013) were employed as the starting compositions to perform the MELTS calculations in this study. Here, these sources are named using author initials and year of publication (e.g., YM20 is Yoshizaki & McDonough, 2020). These compositions are compiled in Table 1 and exhibited in Figure 1.

Since P_2O_5, K_2O, and MnO are not incorporated in the subsolidus peridotite assemblage in pMELTS when feldspar and apatite are absent (Antoshechkina & Asimow, 2018), these elements were treated as trace elements in the initial inputs. Further, the stability field of spinel crystallization is overestimated because in MELTS all Cr is incorporated into spinel (Antoshechkina & Asimow, 2018). Thus, Cr_2O_3 was treated as a trace element in the initial inputs. Other major oxides (SiO_2, TiO_2, Al_2O_3, FeO, MgO, CaO, Na_2O) were renormalized to 100 wt% for each starting composition.

Pressure, Temperature, and Oxygen Fugacity (P, T, fO_2) Conditions

Once a bulk composition constraint is applied, this method allows us to select an "initial guess assemblage" satisfying such composition with fixed variables of T, P, and fO_2 (Asimow & Ghiorso, 1998).

Pressure

The optimized pressure range to run pMELTS was 1–3 GPa (Ghiorso et al., 2002). Asimow (2001) found that pMELTS calculation of the terrestrial peridotite mantle solidus corresponded well with model peridotite solidi of Langmuir et al. (1992) and experimental brackets on the KLB-1 solidus up to ~5 GPa (Takahashi, 1986; Takahashi et al., 1993; Zhang & Herzberg, 1994). But beyond 5 GPa, pMELTS calculations of the mantle solidus increasingly diverge from experimental determinations (Asimow et al., 2004;

TABLE 1. Proposed compositions of bulk silicate Mars and the corresponding mantle solidus mineralogy calculated by pMELTS.

wt%	MA79	OK92	WD94	LF97	BF97	S99	AD04	KC08	T13	M13	YM20
SiO_2	41.6	43.0	44.4	45.4	43.7	47.5	45.5	44.0	43.7	44.7	45.5
TiO_2	0.33	0.24	0.14	0.14		0.10	0.19	0.1[a]	0.14	0.10	0.17
Al_2O_3	6.39	3.48	3.02	2.89	3.13	2.50	3.30	2.50	3.04	3.00	3.59
MnO	0.15	0.22	0.46	0.37		0.40			0.44		0.37
FeO	15.9	15.1	17.9	17.2	18.7	17.7	18.4	17.0	18.1	18.0	14.7
MgO	29.8	34.3	30.2	29.7	31.5	27.3	29.0	33.0	30.5	30.4	31.0
CaO	5.16	2.81	2.45	2.36	2.49	2.00	1.73	2.20	2.43	2.50	2.88
Na_2O	0.10	0.46	0.50	0.98	0.50	1.20	0.46	0.5[a]	0.53	0.50	0.59
K_2O	0.009		0.037	0.110			0.090		0.037		0.043
P_2O_5			0.16	0.18			0.40		0.19		0.17
Total	99.4	99.6	99.3	99.3	100.0	98.7	99.1	98.7	99.1	99.2	99.0
Mg#	77.1	80.3	75.2	75.7	75.2	73.5	74.0	77.7	75.2	75.2	79.1
Fe/Mn	106	69	39	47		44			41		40
Mg/Si	0.92	1.03	0.87	0.84	0.93	0.74	0.82	0.96	0.90	0.87	0.88
Al/Si	0.17	0.09	0.08	0.07	0.08	0.06	0.08	0.06	0.08	0.08	0.09
Ca/Si	0.19	0.10	0.08	0.08	0.09	0.06	0.06	0.08	0.09	0.09	0.10
2 GPa, 1200°C											
Olivine	56	65	53	51	58	39	44	61	57	53	49
Orthopyroxene	1	11	27	22	20	32	41	21	22	27	28
Clinopyroxene	19	16	15	26	16	29	10	14	16	15	17
Garnet	23	8	5	1	6	0.1	5	3	5	5	6
3 GPa, 1300°C											
Olivine	56	65	53	51	58	39	44	61	57	53	49
Orthopyroxene		9	25	22	18	33	39	19	20	25	25
Clinopyroxene	19	17	16	24	17	28	9	15	17	16	17
Garnet	24	10	7	2	8	0.3	8	5	7	7	8
4 GPa, 1350°C											
Olivine	56	65	53	51	58	39	44	61	57	53	49
Orthopyroxene		5	25	21	18	35	40	19	18	24	23
Clinopyroxene	18	20	14	24	16	26	7	14	17	15	17
Garnet	25	10	8	4	9	0.3	9	6	8	8	10
5 GPa, 1400°C											
Olivine	57	65	54	51	58	39	44	61	56	53	49
Orthopyroxene		7	25	23	18	39	39	19	20	25	24
Clinopyroxene	18	16	12	21	15	21	6	13	15	14	16
Garnet	26	11	9	5	9	1	10	7	10	9	11

Note: MA79: Morgan and Anders (1979); OK92: Ohtani and Kamaya (1992); WD94: Wänke and Dreibus (1994); LF97: Lodders and Fegley (1997); BF97: Bertka and Fei (1997)[a]; S99: Sanloup et al. (1999); AD04: Agee and Draper (2004)[a]; KC08: Khan and Connolly (2008); T13: Taylor (2013); M13: Matsukage et al. (2013)[a]; YM20: Yoshizaki and McDonough (2020).
[a]Experimental bulk composition.

Ghiorso et al., 2002). The maximum thickness of Martian crust constrained by topography and gravity is 100 km (Montési, 2003; Zuber et al., 2000), corresponding to a melting pressure of ~1.2 GPa at the base of the Martian crust (Figure 2). Thus, in this study, the pMELTS calculations were performed at 2, 3, 4, and 5 GPa.

Temperature

The temperature corresponding to each pressure was chosen relative to the experimentally determined solidi (Agee & Draper, 2004; Bertka & Fei, 1997; Collinet et al., 2015; Ding et al., 2020; Matsukage et al., 2013) of Martian mantle compositions (Figure 2). The *P–T* profile of these experiments over the pressure interval 0.5–5 GPa is summarized in Figure 2. Two mantle solidi of Mars are shown in Figure 2: one is for WD94 composition (Duncan et al., 2018), and the other is for LF97 composition (Ding et al., 2020). The difference in solidus temperature between WD94 and LF97 compositions is likely due to alkali enrichment in the LF97 composition ($Na_2O + K_2O = 1.05$ wt%) relative to that of WD94 composition ($Na_2O + K_2O = 0.54$ wt%) and other reasons (Ding et al., 2020). Furthermore, in addition to alkali contents, the Mg# of the Martian

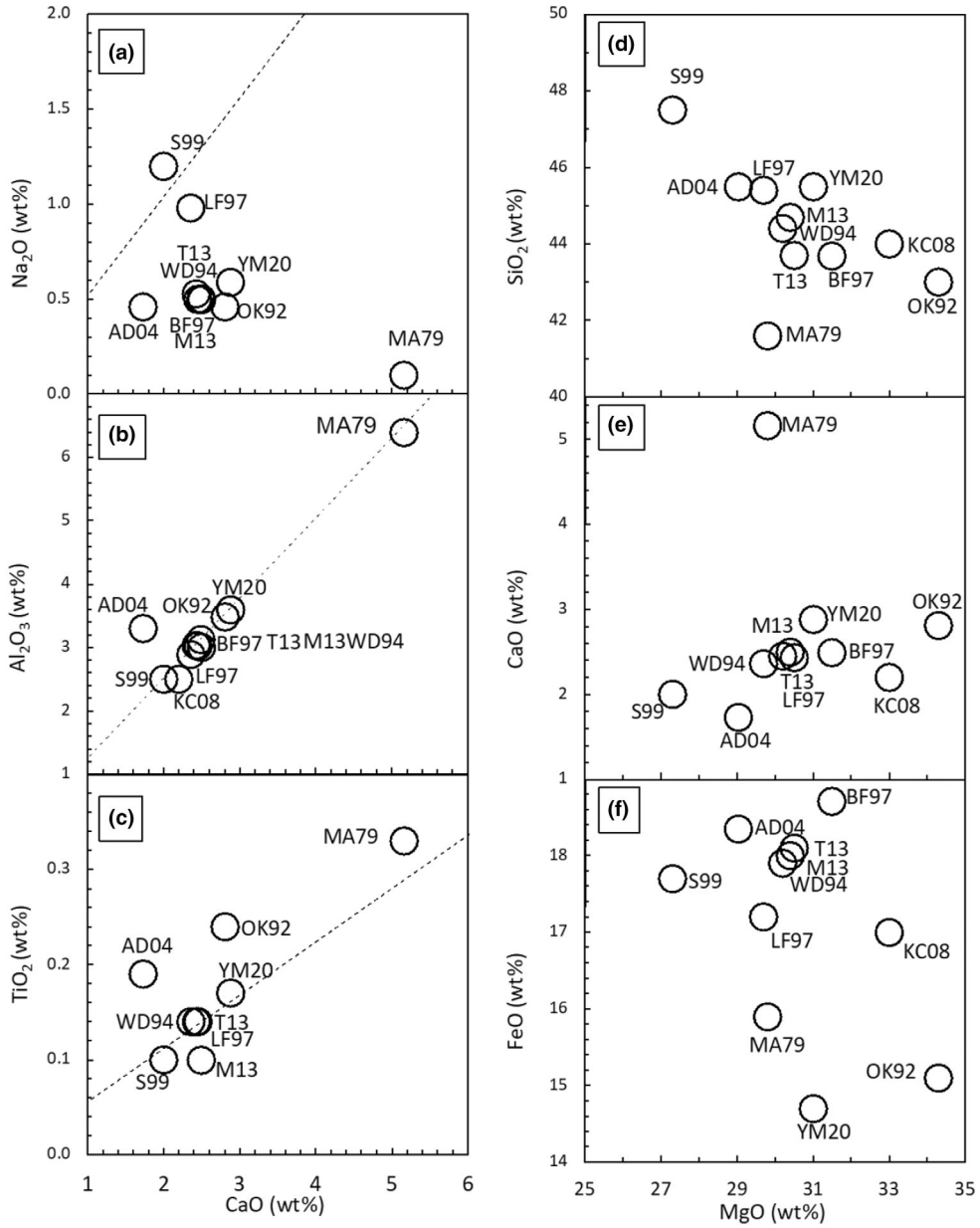

FIGURE 1. (a–c) plots of Na_2O, Al_2O_3, and TiO_2 against CaO; and (d–f) plots of SiO_2, CaO and FeO against MgO of eight published model compositions of BSM (Khan & Connolly, 2008; Lodders & Fegley, 1997; Morgan & Anders, 1979; Ohtani & Kamaya, 1992; Sanloup et al., 1999; Taylor, 2013; Wänke & Dreibus, 1994; Yoshizaki & McDonough, 2020) and three starting compositions of experimental studies (Agee & Draper, 2004; Bertka & Fei, 1997; Matsukage et al., 2013). Sources of compositions are named using author initials and year of publication and used consistently throughout this manuscript. Dash lines in (a–c) indicate chondritic ratios from Anders and Grevesse (1989). The composition of MA79 falls outside of the plotted area in (a–c, e). These compositional models of BSM were employed as the initial chemical composition inputs of pMELTS modeling.

mantle has been demonstrated to be an additional compositional parameter that exerts an influence on the solidus temperature of the mantle (Ding et al., 2020). Given that the Mg# values for the model compositions WD94 and LF97 are identical, it is unlikely that the difference in solidus temperature between these two compositions can be attributed to the influence of Mg#. Two mantle adiabats corresponding to cold and hot Martian mantle with potential temperatures at 1370 and 1450°C (Filiberto & Dasgupta, 2011) are also shown in Figure 2. The combination of the locations of mantle solidi and adiabats shows that the onset of pressure

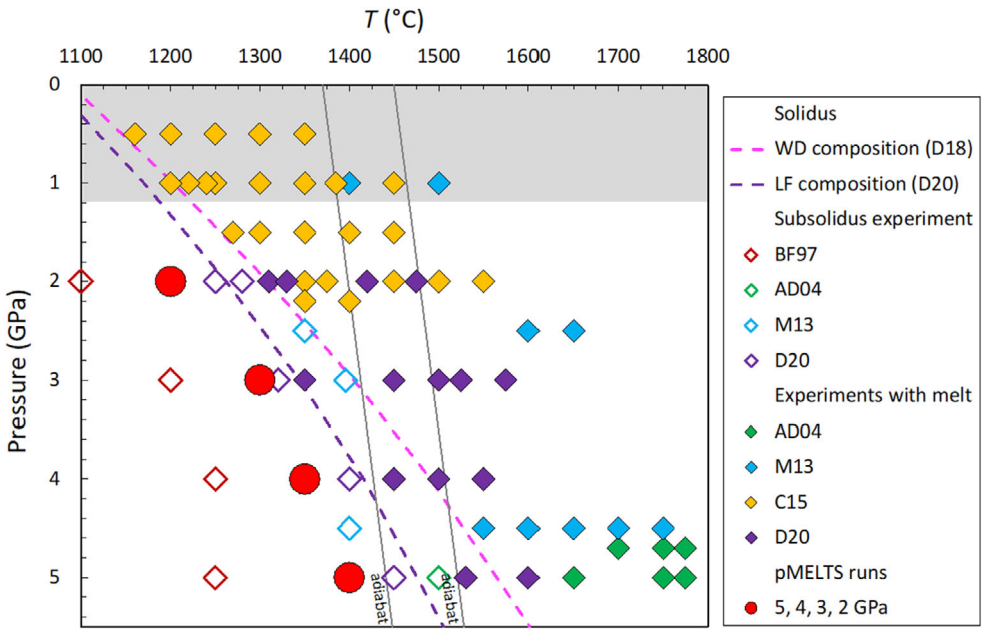

FIGURE 2. *P–T* parameters (filled red circles) of MELTS calculations performed in this study. The solidus of WD94 (Duncan et al., 2018) and of LF97 (Ding et al., 2020); the cold and hot mantle adiabats (Filiberto & Dasgupta, 2011); and the experimental runs (Agee & Draper, 2004; Bertka & Fei, 1997; Collinet et al., 2015; Ding et al., 2020; Matsukage et al., 2013) are compiled to provide insights into the *P–T* parameters used to run MELTS. Gray area shows the thickness of Martian crust constrained by topography and gravity (Montési, 2003; Zuber et al., 2000). Zero liquid was released in MELTS runs performed to calculate solidus phase. (Color figure can be viewed at wileyonlinelibrary.com)

release melting of Martian mantle varies from ~3 to >5 GPa. Since one of the important purposes of this study is to obtain the solidus mineral assemblages in the source region of shergottites, the pMELTS calculations were performed at near-solidus temperatures corresponding to each pressure as presented in Figure 2.

Oxygen Fugacity and Water Contents

Oxygen fugacity (fO_2) affects iron chemistry in the Martian mantle. Studies show shergottites' post-eruptive fO_2 varies widely, correlating with their La/Yb ratios (Herd, 2003; Nicklas et al., 2021; Righter et al., 2008; Wadhwa, 2001). The most reduced sample, QUE 94201, indicates that initial Martian basaltic magmas have fO_2 values around ΔFMQ-3, becoming more oxidized after mantle extraction (Castle & Herd, 2017; Nicklas et al., 2021; Righter et al., 2013). To examine the effect of fO_2 on $Fe^{3+}/\Sigma Fe$, a series of pMELTS calculations were performed here. The results (Figure S3) show that at 1300°C and 3 GPa ($0 \leq \Delta FMQ \leq -4$) yield $Fe^{3+}/\Sigma Fe$ ratios of 0.01–0.07, aligning with redox measurements (Righter et al., 2013). Figure S3 also demonstrates that $Fe^{3+}/\Sigma Fe$ ratios range from 0.01 to 0.02 for ΔFMQ-4 to ΔFMQ-2. These variations are too small to impact mantle mineralogy significantly. Thus, a single fO_2 value (ΔFMQ-3) was used for modeling (Baratoux et al., 2011; El Maarry et al., 2009; Ghosal et al., 1998; Herd et al., 2002).

Hydrous melting of Martian mantle is postulated in pre-magma ocean time (Médard & Grove, 2006; Pommier et al., 2012), whereas melting of dry Martian mantle was postulated for the post-magma ocean history of Mars (e.g., Bertka & Holloway, 1994a, 1994b; Bertka & Fei, 1997; Filiberto & Treiman, 2009). Therefore, water-free pMELTS calculations were performed here. In addition to water, other volatiles such as chlorine (Cl) and fluorine (F) have also been detected in Martian meteorites, providing evidence for their presence in the Martian mantle (Filiberto & Treiman, 2009; Johnson et al., 2008; Shearer et al., 2019). The calculations carried out in this study did not take into account the presence of volatile species such as Cl and F in the Martian mantle, as pMELTS is limited to handling only H_2O as volatile components.

RESULTS

In this section, we present (1) the compositional spectrum of BSM models (Table 1), (2) the solidus mineral modes (Table 1), (3) the composition of each mineral phase (in supplemental data Table S1) at 2, 3, 4, and 5 GPa from pMELTS calculations, and (4) examine

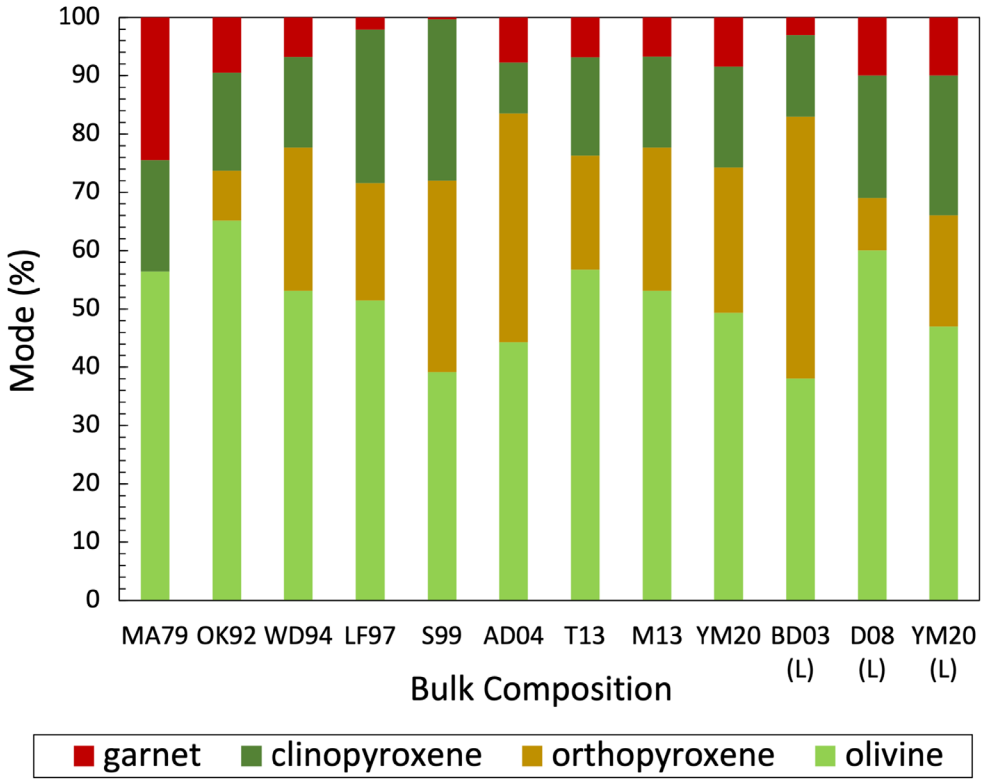

FIGURE 3. The pMELTS outputs of solidus assemblages at 3 GPa for nine BSM compositions adopted as starting compositions. (L) indicates mineralogy of DMM taken from the literature (Borg & Draper, 2003; Debaille et al., 2008; Yoshizaki & McDonough, 2020). (Color figure can be viewed at wileyonlinelibrary.com)

the effect of pressure upon the modes. In Figures 3–6 that follow, data for 3 GPa calculations were taken as representative.

The Compositional Spectrum of BSM Models

The proposed compositional models of BSM are plotted in Figure 1 to examine their geochemical and cosmochemical relationships. BF97 and M13, based on WD94, plot similarly. Martian bulk compositions generally have subchondritic Na_2O, except S99 (Figure 1a). LF97 has nearly twice the Na_2O of other compositions, while MA79 has the lowest Na_2O but the highest CaO (Figure 1a,e). Most compositions have a chondritic Al_2O_3/CaO ratio, except AD04 (super-chondritic) and MA79 (subchondritic; Figure 1b). TiO_2/CaO ratios are mostly chondritic, except for OK92, AD04 (super-chondritic), and M13 (subchondritic) (Figure 1c).

SiO_2 decreases as MgO increases, with S99 highest in SiO_2 and OK92 lowest. Most compositions have MgO between 29 and 31 wt% and SiO_2 between 44 and 45 wt%, but MA79 has lower SiO_2 (~42 wt%) (Figure 1d). CaO content correlates with MgO concentration, with MA79 having higher CaO (5 wt%) than others. Most models have FeO ≥17 wt%, except MA79, OK92, and YM20 (≤16 wt %) (Figure 1e). YM20 has the lowest FeO (14.7 wt%) due to the need for a Martian mantle with Mg# ~80 to produce high Mg# olivine in primitive depleted shergottites (Collinet et al., 2015; Usui et al., 2008; White et al., 2006; Yoshizaki & McDonough, 2020).

The Fe/Mn ratio is diagnostic for Mars. Based on Martian meteorite compositions, the Martian mantle Fe/Mn ratio is ~41 (McSween et al., 2009). The ratios of Fe/Mn of MA79 (105) and OK92 (68) are too high compared to Martian meteorites, due to lower MnO contents (0.15 and 0.22 ppm) compared to other compositions (0.37–0.46 ppm). Other compositions (WD94, LF97, S99, T13, YM20) are within the Fe/Mn range (30–50) constrained by shergottite analyses (Day et al., 2018; Righter, 2017; Yang et al., 2015). BF97, AD04, KC08, and M13 did not report MnO contents. All proposed model compositions were used as starting compositions in pMELTS calculations.

Solidus Mineral Modes

The solidus mineral assemblages for nine modeled Martian compositions at 3 GPa are shown in Figure 3,

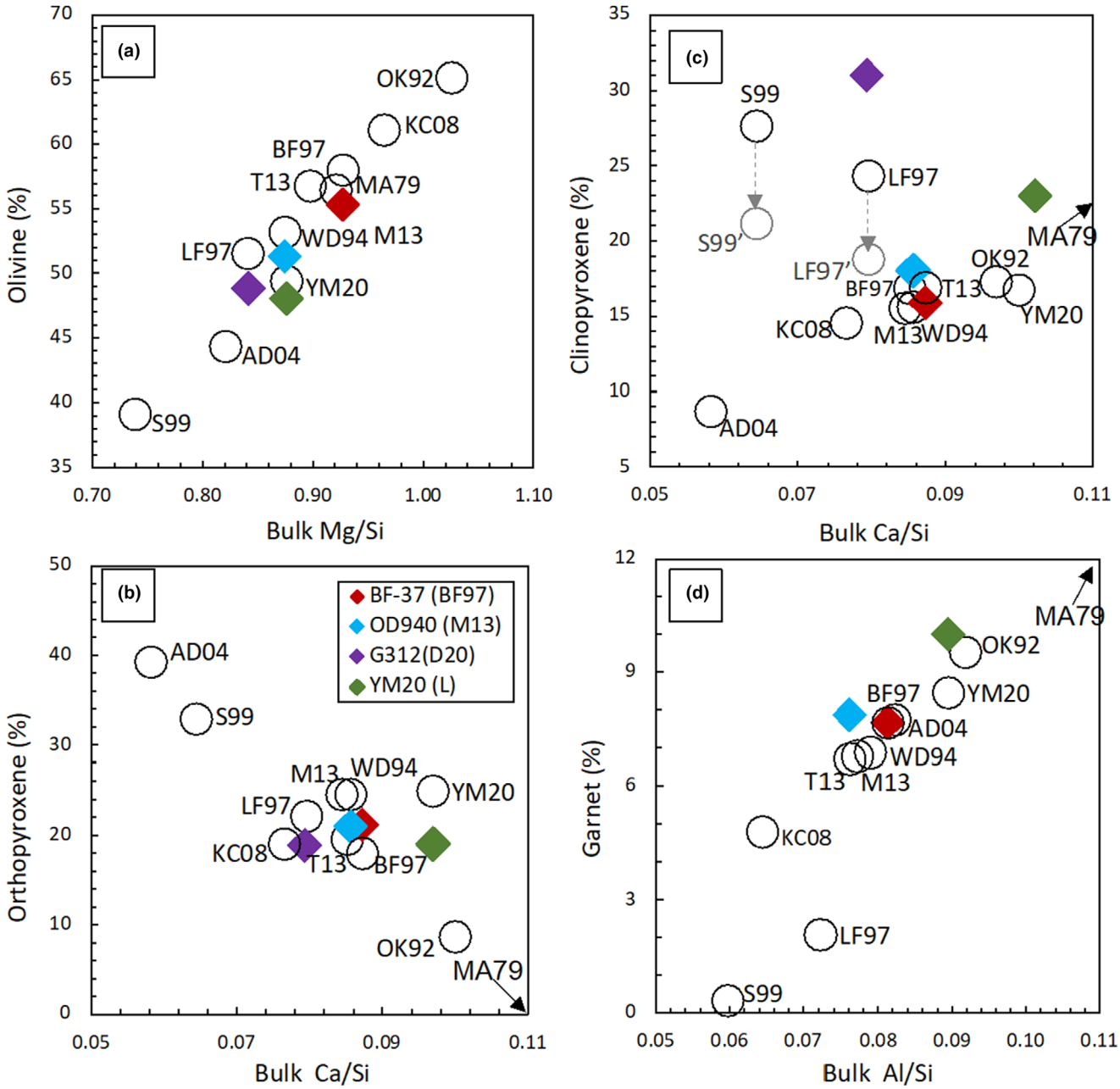

FIGURE 4. Compositional dependence of mantle solidus mineralogy defined by MELTS calculations and experimental runs (Bertka & Fei, 1997; Ding et al., 2020; Matsukage et al., 2013): (a) olivine versus Mg/Si, (b) orthopyroxene versus Ca/Si, (c) clinopyroxene versus Ca/Si, and (d) garnet versus Al/Si. Jadeite-corrected clinopyroxene yielded by S99 and LF97 are presented as S99′ and LF97′ in (c). The composition of MA79 falls outside of the plotted area in (c, d). The mineralogy of BSM from Yoshizaki and McDonough (2020) determined using the Perple_X program is compared with that calculated by MELTS. (Color figure can be viewed at wileyonlinelibrary.com)

including the literature mineralogy of DMM and BSM for comparison (Borg & Draper, 2003; Debaille et al., 2008; Yoshizaki & McDonough, 2020). pMELTS failed for KC08 and BF97 due to a lack of TiO_2 data, so TiO_2 concentrations were computed assuming a chondritic Ti/Ca ratio (Figure 1c). Most compositions yield olivine, clinopyroxene, orthopyroxene, and garnet, except MA79 (no orthopyroxene) and S99 (minimal garnet).

Figure 4 shows correlations between solidus mineral modes and compositional parameters for BSM models. Experimental runs (BF-37, OD940, G312) at 3 GPa used WD94 and LF97 as starting compositions (Bertka & Fei, 1997; Ding et al., 2020; Matsukage et al., 2013).

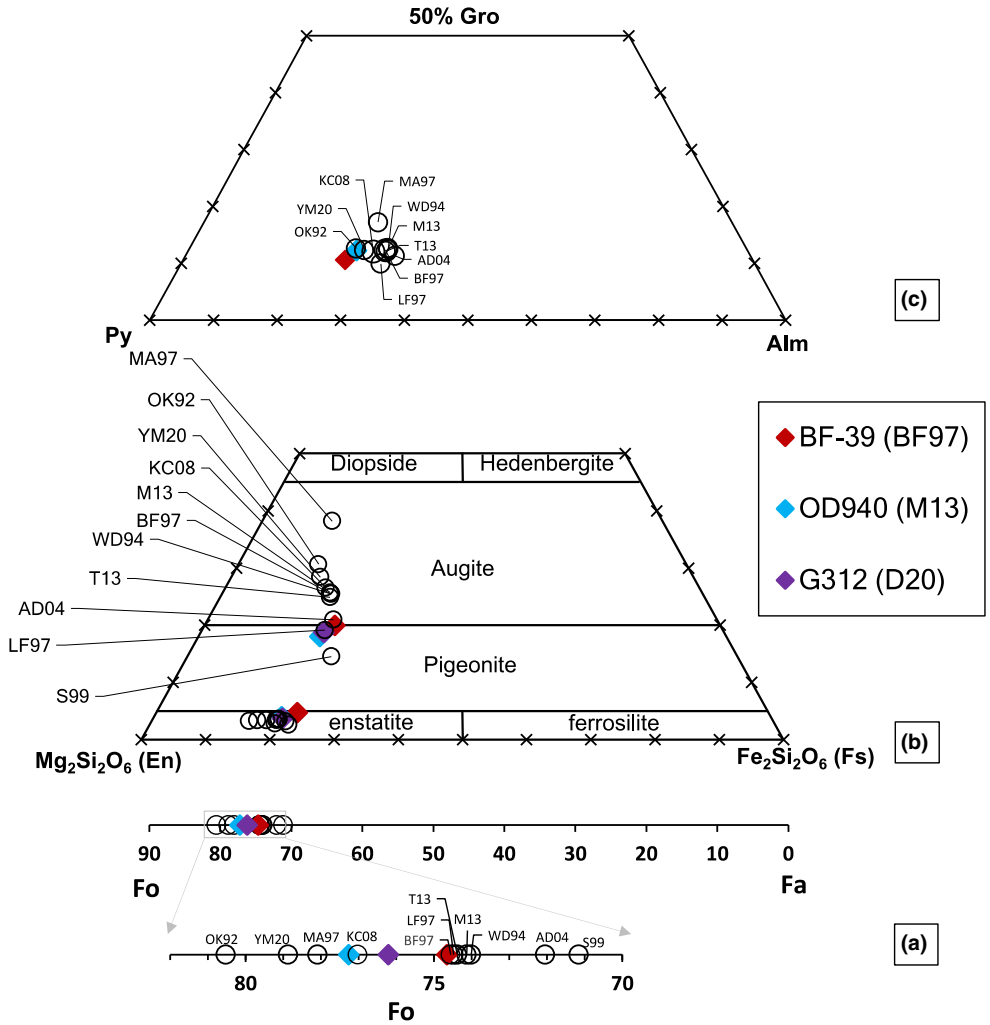

FIGURE 5. The pMELTS outputs of chemical compositions of mineral phases at 3 GPa: (a) Range of olivine compositions (Fo); (b) Quadrilateral plots for pyroxene (after Morimoto, 1988); and (c) Almandine (Alm)-grossular (Gro)-pyrope (Py) plot for garnet. MELTS outputs agree with compositions of experimental run products (Bertka & Fei, 1997; Ding et al., 2020; Matsukage et al., 2013). (Color figure can be viewed at wileyonlinelibrary.com)

Modal mineralogy of BF-37 and OD940 was calculated using GeoBalance (Li et al., 2020), ensuring mass balance by iteratively solving equations based on input data.

Olivine

Olivine modes correlate with bulk Mg/Si ratios (Figure 4a). Calculated olivine modes are consistent with experimental data, varying from 49 to 56 wt%. YM20 has ~5 wt% less olivine than WD94 due to higher Mg# (Collinet et al., 2015; Usui et al., 2008; White et al., 2006; Yoshizaki & McDonough, 2020).

Orthopyroxene

Orthopyroxene modes show an anti-correlation with bulk Ca/Si ratios (Figure 4b). Most compositions have ~20 wt% orthopyroxene. Despite higher Ca/Si, YM20 yields the same orthopyroxene as WD94, indicating other factors like (Fe + Mg)/Si ratio influence orthopyroxene abundance.

Clinopyroxene

Clinopyroxene modes for low Na_2O compositions correlate with Ca/Si ratios (Figure 4c). AD04, with the lowest Ca/Si (0.08), yields the lowest clinopyroxene mode (8 wt%), while MA79, with the highest Ca/Si (0.19), yields the highest mode (19 wt%). S99 and LF97, with high Na_2O, show doubled clinopyroxene modes (>25 wt %) due to a higher jadeite component (Figure 4c). This is consistent with experimental results using LF97 as the starting composition (Ding et al., 2020). This phenomenon arises from a higher jadeite component in high Na_2O compositions (S99 and LF97). LF97 and S99 clinopyroxenes consist of 23 wt% jadeite and 77 wt% Ca-Mg-Fe pyroxenes. After correcting for jadeite, S99

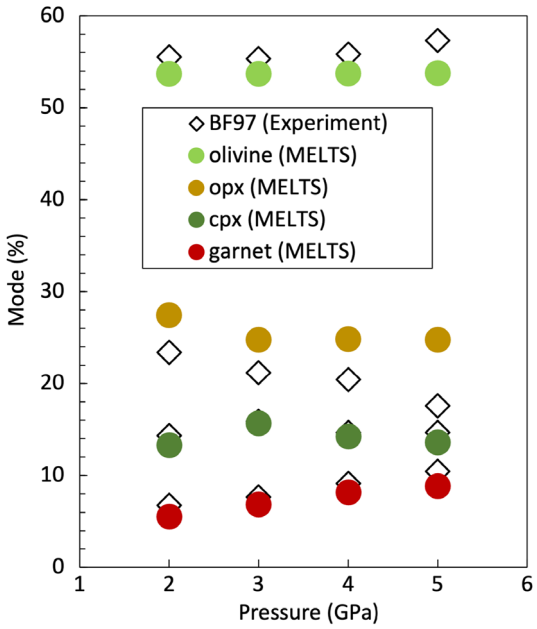

FIGURE 6. Pressure effect on the mode of each phase (olivine, orthopyroxene, clinopyroxene, and garnet). Filled symbols are pMELTS outputs using DW94 as the starting composition from this study. Open symbols are run products of the experiments using DW94 as the starting composition from Bertka and Fei (1997). Modes of run products from Bertka and Fei (1997) were calculated using the GeoBalance program (Li et al., 2020). pMELTS calculations agree well with experimental data, and the effect of pressure on the solidus mineral mode between 2 and 4 GPa is minor. (Color figure can be viewed at wileyonlinelibrary.com)

clinopyroxene mode is ~10 wt% higher and LF97 is ~3 wt% higher than other compositions (Figure 4c).

Garnet

Garnet modes correlate with bulk Al/Si ratios (Figure 4d), consistent with experimental modes.

Chemical Compositions of Solidus Mineral Phases

The chemical compositions of solidus mineral phases (olivine, orthopyroxene, clinopyroxene, and garnet) calculated by pMELTS are given in Table 1. The 3 GPa results are presented in Figure 5 and in Figures S1 and S2.

The solidus olivines have compositions of $Fo_{70\text{-}81}$ from the pMELTS calculation, which is in the same range as the compositions of olivine produced by 3 GPa experimental runs (Bertka & Fei, 1997; Ding et al., 2020; Matsukage et al., 2013; Figure 5a). The Fo compositions calculated for solidus olivines reflect the Mg# of model compositions of bulk Mars (Figure S1). The systematics of pyroxene quadrilateral components, Wollastonite–Enstatite–Ferrosilite (Wo-En-Fs), in calculated pyroxene compositions are illustrated in (b). All orthopyroxene compositions calculated by pMELTS fall in the enstatite endmember ($En_{82\text{-}77}$), and the clinopyroxene compositions span from the pigeonite to the augite zone (Figure 5b). The pMELTS calculated composition of garnet corresponding to each model composition of bulk Mars is shown in Figure 5c, which are generally in good agreement (± 2 wt%) with the experimental garnet compositions (Bertka & Fei, 1997; Matsukage et al., 2013).

The Effect of Pressure on Calculated Solidus Assemblages

The variation of solidus modes yielded by the WD94 composition against pressure (2–5 GPa) is shown in Figure 6. The experimentally determined solidus mode from Bertka and Fei (1997) using WD94 as a starting composition is shown for comparison (Figure 6). The effect of pressure on the calculated pMELTS solidus mineral mode between 2 and 4 GPa is minor. The olivine mode (~ 55 wt%) remains constant from 2 to 4 GPa in both pMELTS calculations and experimental results (Bertka & Fei, 1997). The experimental orthopyroxene mode drops gradually from 23 to 20 wt% as pressure increases from 2 to 4 GPa (Bertka & Fei, 1997), while pMELTS calculated mode drops from ~27 to ~25 wt% as pressure increases from 2 to 3 GPa, and keeps consistent at 3–4 GPa. Both pMELTS calculated and experimental clinopyroxene modes (Bertka & Fei, 1997) vary between ~13 and ~16 wt % but is not correlated with pressure in the range of 2–4 GPa. Both pMELTS calculated and experimental garnet modes (Bertka & Fei, 1997) increase from ~6 to ~9 wt% as pressure increases from 2 to 4 GPa. Overall, mineral modes are approximately constant with pressure from 2 to 5 GPa, with a small decrease in orthopyroxene (~3 wt%) for a similar increase in garnet mode.

In general, pMELTS calculations agree well with experimental data within the pressure interval 2–4 GPa for olivine, clinopyroxene, and garnet (±5 wt%). The pMELTS calculated modes of orthopyroxene consistently exhibit a ~4 wt% higher value compared to the experimental orthopyroxene modes (Figure 6). At 5 GPa, the pMELTS calculated mineral modes deviate increasingly from the experimental data (Figure 6). This is because the pMELTS program is unable to match actual compositions outside of the calibrated pressure range (Asimow et al., 2004; Balta & McSween, 2013).

DISCUSSION

The Accuracy of pMELTS at Determining the Solidus Mineralogy of the Martian Mantle

Comparison with Experimental Compositions

The pMELTS calculations are compared with the near-solidus experimental data of Martian mantle

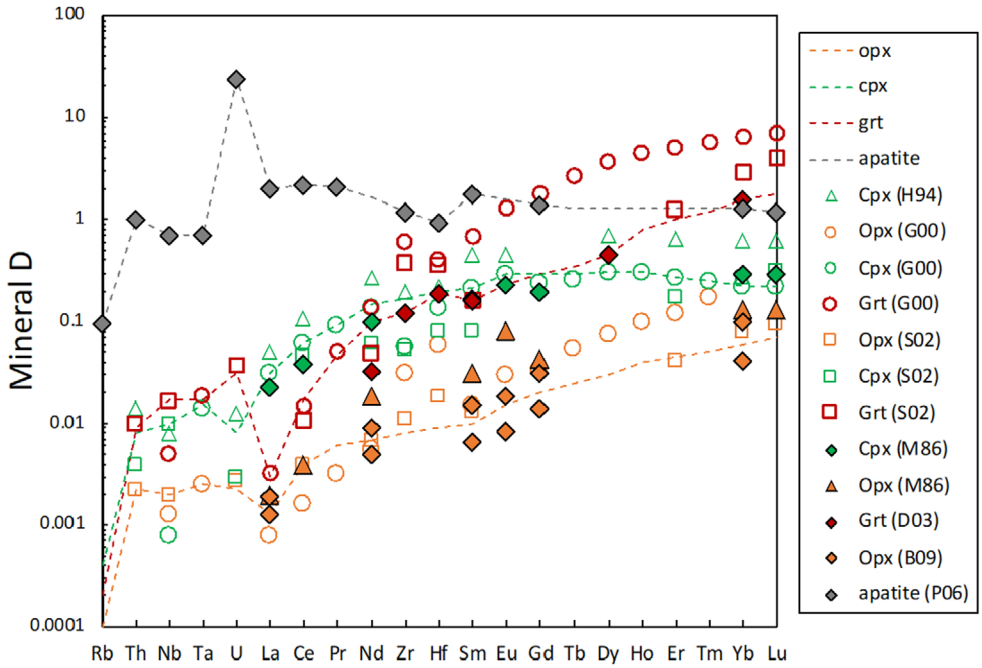

FIGURE 7. Experimental determined partition coefficients (D) of trace elements between minerals and melts. Data from McKay et al. (1986), Draper et al. (2003), and Blinova and Herd (2009) are obtained on shergottite compositions (filled symbols). Data from Hauri et al. (1994), Green et al. (2000), and Salters et al. (2002) were obtained on terrestrial basaltic compositions. The trace elemental D values between apatite and silicate melts are from Prowatke and Klemme (2006). (Color figure can be viewed at wileyonlinelibrary.com)

compositions to assess the accuracy of pMELTS calculations (Figures 7 and 8; Figures S1 and S2). Three 3 GPa experimental runs BF-37 (Bertka & Fei, 1997), OD940 (Matsukage et al., 2013), and G312 (Ding et al., 2020) were plotted with pMELTS calculated modes (Figure 7), showing pMELTS calculated modes are in good agreement (±3 wt%) with experimental modes.

In Figure 7 and Figures S1 and S2, the solidus mineral compositions determined by pMELTS were compared with EMP analysis of minerals in the experimental run products of BF-37 (Bertka & Fei, 1997), OD940 (Matsukage et al., 2013), and G312 (Ding et al., 2020). Despite some minor inconsistencies, the calculations of solidus assemblages (modes and compositions) using the pMELTS program are in good agreement with that of experimental studies of Martian mantle compositions.

Comparison Between Perple_X/stx11 and pMELTS

Yoshizaki and McDonough (2020) used the stx11 thermodynamic parameter of Stixrude and Lithgow-Bertelloni (2011) in the modeling code Perple_X (Connolly, 2009) to calculate the mineralogy of the Martian mantle based on their estimate (YM20) of its bulk composition. Here, we conduct a comparative analysis of the solidus mineralogy for YM20 composition as obtained by pMELTS in this study and as determined by the Perple_X/stx11, as reported by Yoshizaki and McDonough (2020). The calculated phase modes of olivine (49 wt% vs. 48 wt%), pyroxene (42 wt% vs. 42 wt%), and garnet (8.5 wt% vs. 10 wt%) are consistent between pMELTS and Perple_X/stx11. The orthopyroxene to clinopyroxene ratio obtained by pMELTS (25 wt%: 17 wt%) differs from that obtained by Perple_X/stx11 (19 wt%: 23 wt%). A higher proportion of clinopyroxene with lower Ca content is yielded by pMELTS compared with Perple_X/stx11. The impact of this mineralogical difference on the bulk D will be discussed below.

Implications for Trace Elemental Partitioning in the Martian Mantle

A potential test of the proposed compositions of bulk Martian mantle could be made by predicting the trace element composition of basalts derived by melting these hypothetical mantle compositions. Taking the mineral modes of the existing set of bulk Martian mantle compositions as an input (Table 1), the bulk partition coefficients of trace elements of each mantle source were calculated. The bulk trace element partition coefficient (D_E) between mantle assemblage and melt is given by:

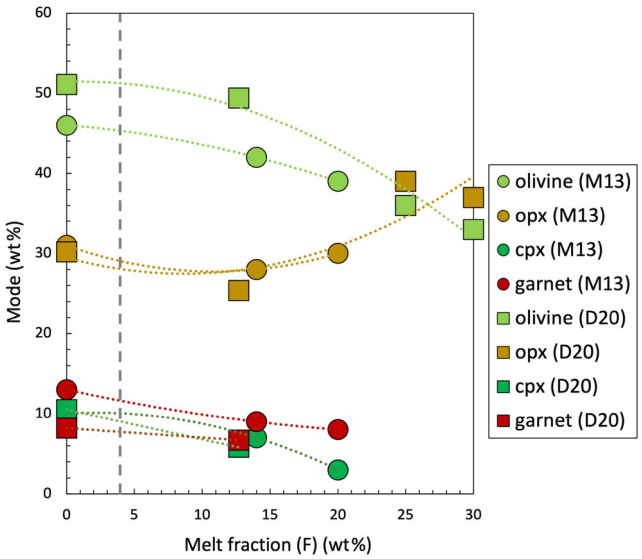

FIGURE 8. The change in mineral modes of melting residues as a function of the melt fraction. Data are from experimental studies (Ding et al., 2020; Matsukage et al., 2013). Dash line indicates partial melting degree $F = 4$ wt% needed to extract Martian crust (Humayun et al., 2013). Alterations in the residue modes are minimal following 4% melting. (Color figure can be viewed at wileyonlinelibrary.com)

$$\text{bulk } D_E = \sum_0^n D_i f_i \quad (1)$$

where D_i is the mineral melt partition coefficient for each mineral, and f_i is the mass fraction (modal abundance) of that mineral in the assemblage. Several experimental studies have focused on the determination of trace element partition coefficients (D) on shergottite compositions. McKay et al. (1986) determined Rare Earth Element (REE) Ds between pyroxenes and synthetic shergottite melts in one atmosphere. They found that REE Ds exhibit a strong positive correlation with pyroxene Wo content. Draper et al. (2003) determined garnet-melt Ds for trace elements from 5 to 9 GPa in the Homestead L5 ordinary chondrite bulk composition. Blinova and Herd (2009) determined REE Ds between olivine, pyroxene, and melts of the Yamato 980,459 composition 1–2 GPa and 1350–1650°C corresponding to the generation of Martian basaltic melts. These D values were compiled in this study and are shown in Figure 7 and Table S2. Additionally, experimentally determined Ds of trace elements on terrestrial basaltic compositions are also shown in Figure 7 for the purpose of comparison (Green et al., 2000; Hauri et al., 1994; Salters et al., 2002). As shown in Figure 7, trace element Ds determined in Martian (filled symbols) and terrestrial (open symbols) compositions overlap. One noticeable offset is that garnet-melt Ds of heavy REE (HREE) from Green et al. (2000) are an order of magnitude higher than that from Draper et al. (2003). Although the garnet-melt D values of HREE show a tendency to elevate as pressure increases from 2 to 10 GPa (Draper et al., 2003 and reference therein), this tendency was not observed in the experiments from 2 to 7.5 GPa from Green et al. (2000). Further, the experimental data of D_{HREE} between garnet-melt at 2 and 5 GPa (Nicholls & Harris, 1980; Salters & Longhi, 1999; van Westrenen et al., 2001) compiled in Draper et al. (2003) are variable (e.g., D_{Lu} varies from 1.7 to 10). In Implications for Partial Melts Derived from the Martian Mantle section, we used D_{HREE} between garnet-melt from Draper et al. (2003). For HREEs not included in Draper et al. (2003), their D values were calculated based on the ratios of their D values to D_{Yb} as determined in Green et al. (2000). The Ds of highly incompatible elements (Rb, Th, Nb, Ta, U, and K) were all taken from experimental studies using terrestrial compositions because such D values are not available from experimental studies on Martian compositions. The trace element Ds of orthopyroxene-, clinopyroxene-, and garnet-melt used to obtain bulk Ds of Martian mantle are shown in Figure 7 (dash lines). The D's for olivine are small enough to be neglected.

As shown in Figure 7, in orthopyroxene and garnet, Th, Nb, U, and K are slightly more compatible relative to La. But in clinopyroxene, these elements are more incompatible relative to La. Thus, the relative bulk Ds of these elements against D_{La} are sensitive to the modes of orthopyroxene + garnet versus that of clinopyroxene. Similarly, HREEs are significantly more compatible relative to La in orthopyroxene and garnet but are comparable to La in their compatibilities in clinopyroxene (Figure 7). Therefore, relative D_{HREE}/D_{La} are sensitive to the mantle modes of orthopyroxene + garnet against clinopyroxene. Thus, melts derived from source regions with low garnet (e.g., LF97 and S99) are expected to be more enriched in highly incompatible elements (e.g., Th, Nb, U, K) and HREE. Whereas melts derived from source regions with high garnet (e.g., MA79) or high garnet + orthopyroxene (e.g., AD04) are expected to be less enriched in these elements relative to a reference composition such as WD94 or YM20. From a trace element perspective, the Ca content of pyroxene and its mode both increase the partition coefficients of REE (e.g., McKay et al., 1986). Thus, the observed offsets in proportion and composition of clinopyroxene yielded from a single composition (e.g., YM20) by two thermodynamic programs (pMELTS vs. stx11) will lead to a compensation of errors when calculating a bulk D for the pyroxene compositions.

Recent experimental research (Payrè & Dasgupta, 2022) indicates that BSM with a bulk P_2O_5 concentration of 0.5 wt% produce a minor quantity of apatite (0.3 wt%). In contrast, BSMs with a bulk P_2O_5 concentration of less

than 0.2 wt% exhibit no presence of apatite. In BSM models where P_2O_5 is available, the majority (WD94, LF97, T13, YM20) estimate its concentration to be less than 0.2 wt%. One BSM model (AD04) exhibits a P_2O_5 concentration of 0.4 wt%. The experimentally determined partition coefficients (Prowatke & Klemme, 2006) between apatite and silicate melts are presented in Figure 7. This shows that elements from Rb to Nd, which are highly incompatible in pyroxenes and garnet, are more compatible in apatite. Most notably, U displays a D value in apatite that is approximately two orders of magnitude greater than its corresponding value in pyroxene and garnet. While the presence of minor amounts (0.03 wt%) of apatite exerts a negligible influence on the bulk D values of most trace elements, its impact on the bulk D of U is substantial. Consequently, this leads to a pronounced depletion of U in the liquid originating from a source bearing apatite as a residual phase.

Implications for Partial Melts Derived from the Martian Mantle

In this section, the influence of mantle mineralogy on the composition of partial melts derived from the mantle is explored and compared with published compositions of shergottites. A DMM was selected as the source region for depleted shergottites. Here, the depleted mantle was considered as a complementary residue resulting from the extraction of a primary Martian crust represented by the composition of NWA 7533 and paired meteorites (Humayun et al., 2013) from BSM.

The proposed compositions of trace elements of BSM are summarized in Figure S4. The models WD94, T13, and YM20, all based on Martian meteorite data, exhibit remarkably similar compositions, whereas MA79 has higher total refractory element composition and exhibits Nb-Ta and Zr-Hf systematics that are no longer state of the art. Although similar in most elements, LF97 displays a high Rb content because this composition is derived directly from combinations of chondrite types that have higher moderately volatile element contents than Martian bulk compositions derived from shergottites (WD94, T13, YM20).

The starting composition (C_0) of BSM is taken as YM20. The bulk partition coefficients (D) were calculated using YM20 mineralogy (Table 1) and elemental Ds for each mineral from literature sources (see above). The elemental compositions of melts (C_l) were calculated from the batch melting equation:

$$\frac{C_l}{C_0} = \frac{1}{D \times (1-F) + F} \quad (2)$$

where F is the melt fraction. Experimental melting of Martian mantle compositions (Ding et al., 2020; Matsukage et al., 2013) shows that the changes in mineralogy induced by <10 wt% partial melting do not perceptibly modify the mineralogical modes of the solidus residue (Figure 8), justifying the use of modal melting. The results of the modeling are shown in Figure 9 where the modeled melt compositions are compared with three estimates of the bulk compositions of Martian breccia (Agee et al., 2013; Humayun et al., 2013; Wittmann et al., 2015). This modeling shows that melts derived from $F = 4$ wt% partial melting of a BSM with YM20 composition fit the trace elemental pattern observed in the bulk composition of the Martian breccia. The calculation above shows that the composition of Martian highlands crust is consistent with the extraction of 4 wt% partial melt from the BSM composition, which aligns with previous studies, such as 2–8 wt% proposed in Norman (1999) and ~4 wt% proposed in Humayun et al. (2013). This finding enables us to apply a mass balance calculation to constrain the composition of DMM sources (Figure 9 and Table 2) by assuming that DMM is compositionally complementary to the Martian highlands crust and that NWA 7533 is representative of the bulk crustal composition (Agee et al., 2013; Humayun et al., 2013).

The compositions of melts derived from DMM were modeled using Equation (2). Here, the starting composition (C_0) corresponds to the composition of DMM as shown in Figure 10. The degree of partial melting (F) was varied from 5 to 20 wt%. Since the low degree of partial melting (4 wt%) required for extraction of the Martian crust does not significantly change the modal mineralogy of the solid residue (Figure 8), the modal mineralogy of DMM is consistent with that of BSM (Table 1). To assess the effect of the amount of garnet in the source, the garnet modes of DMM were arbitrarily assigned at 0, 5, 10, and 15 wt%. As the modal proportion of garnet was increased, the modal proportion of orthopyroxene was decreased, with the modes of other minerals remaining constant. The compositions of partial melts originating from DMM with varying modal garnet proportions were calculated, and these computed melts are compared with the analyses of depleted shergottites in Figure 10.

As shown in Figure 10a–d, the compositions of melts derived from DMM characterized by various garnet modes (0, 5, 10, and 15 wt%), exhibit indistinguishable Rb to Hf compositions. This is because within the partial melting degree range of 5–20 wt%, the concentrations of highly incompatible to incompatible elements in the liquids are primarily governed by the values of C_0 and F.

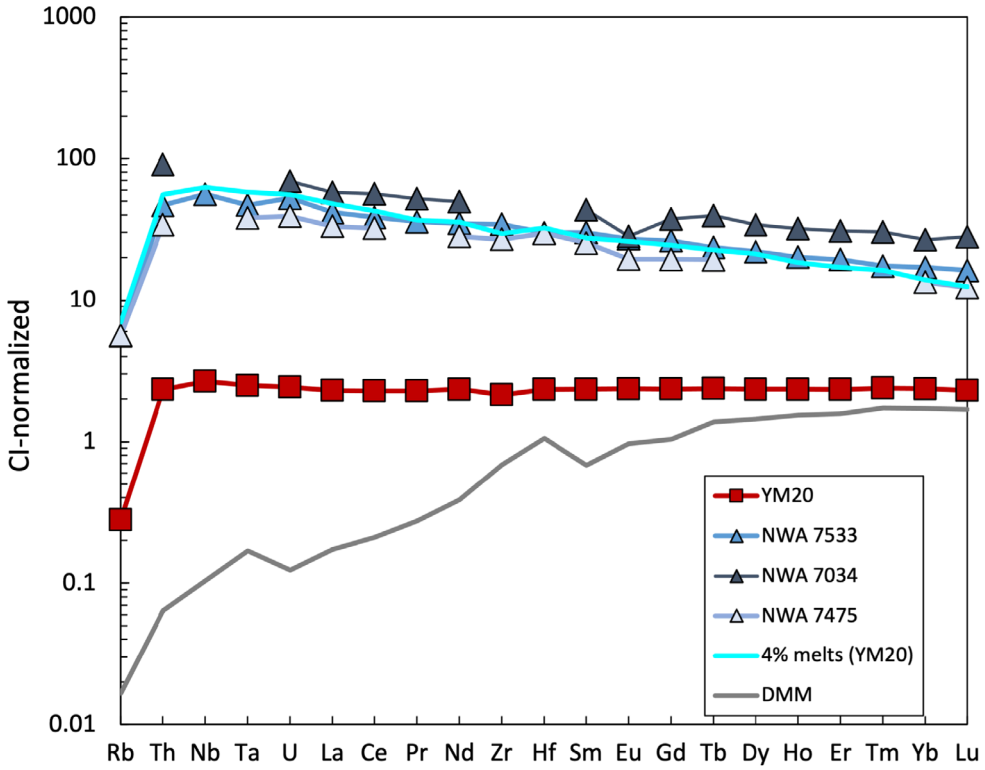

FIGURE 9. The determination of the composition of a representative Depleted Mars Mantle (DMM). The composition of a melt derived by 4% partial melting of a primitive mantle composition (Yoshizaki & McDonough, 2020) matches the compositions of Martian breccia (Agee et al., 2013; Humayun et al., 2013), taken here to represent the average Martian crust. The composition of DMM was determined by mass balance calculations assuming it to be a residue of crustal extraction. (Color figure can be viewed at wileyonlinelibrary.com)

Hence, while the relative D values of Th, Nb, and U with respect to La exhibit sensitivity to the garnet mode of the mantle source mineralogy, the concentrations of these elements in the liquids derived from source regions with different garnet modes cannot be distinguished. In contrast, the patterns observed in moderately incompatible heavy rare earth elements (HREEs), ranging from Gd to Lu, in the partial melts predictably exhibit sensitivity to the proportion of garnet present in the mantle source. Noticeably, the modeled composition of partial melts derived from the source region with 5–10 wt% garnet mode demonstrates the closest agreement with the analyses of depleted shergottites (Figure 10c,d).

Hence, the source mineralogy with low (<2 wt%) garnet mode (such as LF97, S99) or high garnet (>20 wt %) or garnet + orthopyroxene (>50 wt%) mode (such as AD04) do not generate partial melts that correspond to the compositional analyses of shergottites. The source mineralogy derived from the WD94, T13, and YM20 models, exhibiting an intermediate garnet mode ranging from 6 to 9 wt%, all yield melt compositions consistent with the source mantle mineralogy of shergottites. As mentioned in the preceding section, the presence of a minor quantity of apatite (0.3 wt%) significantly elevates the bulk D value for U (Prowatke & Klemme, 2006), given its high compatibility in apatite (Figure 7). Yet, U depletion was not discerned in depleted shergottites (Figure 10), suggesting a mantle source characterized by a bulk P_2O5 content of less than 0.2 wt%. In summary, a DMM derived from a bulk composition like that of YM20, WD94, or T13 with 6–9 wt% garnet provides the best HREE match to depleted shergottite compositions.

In a recent publication, Collinet et al. (2023) estimated the major compositions of source regions of shergottites using MAGMARS melting model. They hypothesized that the geochemical characteristics of shergottites can be best explained through melting processes in a mantle source that has experienced significant depletion as a result of prior high-degree melting ($F = 20$ wt%) events within the spinel stability field (at pressures <2 GPa). Such conditions would lead to considerable alterations in the mineral composition of the shergottite source region, characterized by a depletion in aluminum, a depletion of garnet, and an enrichment in olivine. The mineralogical composition of the source proposed by Collinet et al. (2023) appears to be in contract with our proposed source mineralogy, which posits a garnet content ranging from 6 to 9 wt%. As shown in Figure 10, a garnet-free mantle is unable to produce

TABLE 2. Incompatible element abundances (ppm) in BSM (YM20) and DMM.

Conc. (ppm)	YM20[a]	DMM
Rb	1.2	0.038
Th	0.0678	0.0019
Nb	0.64	0.025
Ta	0.0339	0.0023
U	0.018	0.0009
La	0.546	0.041
Ce	1.40	0.129
Pr	0.212	0.025
Nd	1.07	0.177
Zr	8.20	2.62
Hf	0.241	0.109
Sm	0.347	0.101
Eu	0.133	0.055
Gd	0.468	0.207
Tb	0.0858	0.050
Dy	0.578	0.354
Ho	0.128	0.084
Er	0.374	0.251
Tm	0.0590	0.043
Yb	0.381	0.277
Lu	0.0566	0.041

[a]Incompatible element abundances in BSM from Yoshizaki and McDonough (2020).

partial melts that are consistent with the trace element patterns observed in shergottites. In the context of these models, identifying a discrepancy between the requirements of trace elements and those of major elements presents a particularly intriguing prospect, necessitating further investigation.

Mineralogical Constraints on the Composition of the Martian Mantle

Compositional models (WD94, T13, YM20) calibrated against Martian meteorite data: The mineralogical modes produced by these compositional models exhibit a constrained range of mineral abundances: garnet constitutes 6–9 wt%, clinopyroxene ranges between 15 and 17 wt%, orthopyroxene varies from 20 to 25 wt%, and olivine accounts for 48–56 wt%. Expectedly, these compositional models yield mineralogical modes that are more consistent with trace element abundances in shergottites than other models.

Compositional models (MA79, LF97, S99) based on chondritic meteorites: MA79 composition barely produced any orthopyroxene due to its high Ca/Si ratio and the garnet proportion is over 20 wt% in its mineral mode due to the high Al_2O_3 content. Since S99 and L97

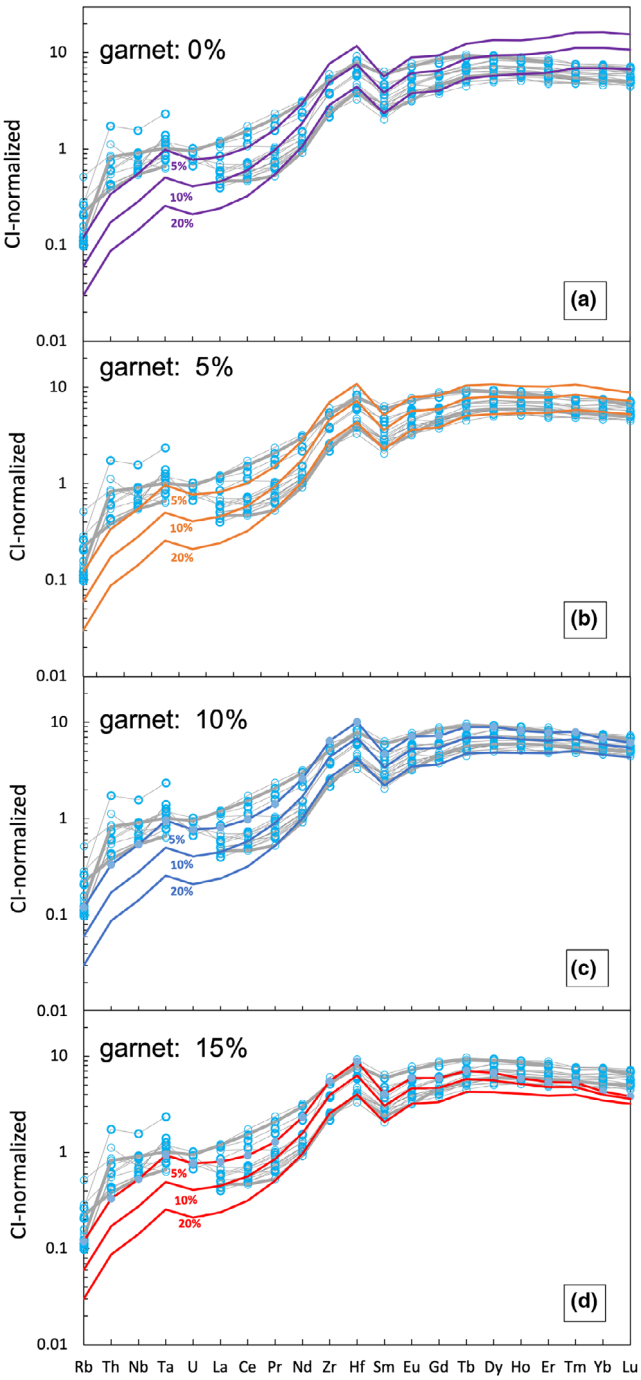

FIGURE 10. A comparison of the compositions of depleted shergottites with compositions of calculated partial melt from Depleted Mars Mantle (DMM) with variable modal garnet (0–15 wt%). (a) Melts from a DMM source with 0 wt% garnet; (b) melts from a DMM source with 5 wt% garnet; (c) melts from a DMM source with 10 wt% garnet; and (d) melts from a DMM source with 15 wt% garnet. The percentage values accompanying the modeled liquid compositional patterns denote the melting degrees within the mantle source. (Color figure can be viewed at wileyonlinelibrary.com)

overestimated volatile contents such as Na2O, they produced ~20 wt% jadeite in clinopyroxene phases. These models fail to produce appropriate Rb/Th for Martian mafic rocks, a ratio that is not sensitive to mineral mode.

Geophysical models (OK92 and KC08): As shown in Figure 1, both OK92 and KC08 have chondritic or near-chondritic Al_2O_3/CaO ratio (Figure 1b), but both models are on the higher MgO end of the compositional spectrum (Figure 1d–f). Since the mantle olivine mode closely correlates with bulk Mg/Si ratio, the compositions OK92 and KC08 yielded higher near-solidus modal olivine (>60 wt%) than that yielded by other compositions. The modal garnet of OK92 (9.5 wt%) is compatible with shergottite data, while that of KC08 (>5 wt%) is too low.

Magma Ocean Cumulate models (BD03, D08): The mineralogy of DMM as cumulates of a deep (1350 km) MMO has been investigated in previous studies by both forward modeling (Borg & Draper, 2003) and inverse modeling (Debaille et al., 2008) approaches. Mineral modes for both compositional models are presented in Figure 3 for the purpose of comparison against other models. The forward approach (BD03; Borg & Draper, 2003) constrained the crystallized cumulates of MMO based on the phase relations determined in high-pressure experimental studies (e.g., Bertka & Holloway, 1994a, 1994b; Draper et al., 2003). The inverse approach determined the DMM mineralogy based on the isotopic systematics of melts (i.e., depleted shergottites) derived from DMM (D08; Debaille et al., 2008). Notably, BD03 exhibits a relatively low modal proportion of garnet (~3 wt%), whereas D08 yields the higher garnet modal (10 wt%).

CONCLUSIONS

1. The solidus mineral modes calculated by the pMELTS program are in good agreement with mineral modes calculated with the Perple_X program and with experimentally determined mineral modes of Martian mantle compositions equilibrated at 2–4 GPa.
2. Compositional models that are calibrated against Martian meteorite data (e.g., WD94, T13, YM20) yield mineral modes that have a narrow range of mineral abundances: garnet (6–9 wt%), clinopyroxene (15–17 wt%), orthopyroxene (20–25 wt%), and olivine (48–56 wt%). In contrast, compositional models based on chondritic meteorites (MA79, LF97, S99) yield much wider ranges of mineral abundances.
3. Geophysical models (e.g., OK92) yield compositions that are more olivine-rich than those based on Martian meteorite data (e.g., WD94, YM20).
4. In principle, magma ocean cumulates could yield very diverse mineral modes (BD03 vs D08), but the mineral abundances reported in existing cumulate models for the sources of depleted shergottites are within the range of the compositional spectrum of other bulk Martian mantle models.
5. Removal of low-degree (<10 wt%) melt from a BSM to form a DMM does not significantly change the mineralogy, implying that the currently known types of shergottites (enriched, intermediate, and depleted) are likely to be derived from sources with similar mineral modes but different bulk chemical compositions.
6. Combining the solidus mineral modes obtained in this study with experimentally determined mineral *D*s shows that DMM mineral modes are constrained by the compositions of depleted shergottites to have a garnet mode ranging from 6 wt% to 9 wt%.
7. Compositional models based on Martian meteorites (WD94, T13, YM20), magma ocean cumulates (D08), and geophysical models (OK92) yielded garnet modes consistent with the sources of depleted shergottites. Models based on chondritic mixtures or chondritic components yielded garnet modes either too low (LF97, S99) or too high (MA79).

Acknowledgments—We thank Tony Irving, Roger H. Hewins, and Brigitte Zanda for discussions on this manuscript and for contributing their insights on Martian meteorites. This manuscript benefitted greatly from reviews by Brian Balta, Daniel Astudillo Manosalva, and an anonymous reviewer. We thank Cyrena Goodrich for editorial handling of the manuscript. This research was supported by the National Aeronautics and Space Administration Solar Systems Workings program (NNX16AP98G). The National High Magnetic Field Laboratory is supported by the National Science Foundation through NSF/DMR-1644779 and the State of Florida.

Editorial Handling—Dr. A. J. Timothy Jull

REFERENCES

Agee, C. B., and Draper, D. S. 2004. Experimental Constraints on the Origin of Martian Meteorites and the Composition of the Martian Mantle. *Earth and Planetary Science Letters* 224: 415–429.

Agee, C. B., Wilson, N. V., McCubbin, F. M., Ziegler, K., Polyak, V. J., Sharp, Z. D., Asmerom, Y., et al. 2013. Unique Meteorite from Early Amazonian Mars: Water-Rich Basaltic Breccia Northwest Africa 7034. *Science* 339: 780–85.

Anders, E., and Grevesse, N. 1989. Abundances of the Elements: Meteoritic and Solar. *Geochimica et Cosmochimica Acta* 53: 197–214.

Aoudjehane, H. C., Avice, G., Barrat, J. A., Boudouma, O., Chen, G., Duke, M. J. M., Franchi, I. A., et al. 2012. Tissint Martian meteorite: A fresh look at the interior, surface, and atmosphere of Mars. *Science* 338: 785–88.

Antoshechkina, P., and Asimow, P. D. 2018. AlphaMELTS Software Manual (Version 1.9) https://magmasource.caltech.edu/alphamelts/1/alphamelts_manual.pdf.

Asimow, P. D. 2001. Calculation of Peridotite Partial Melting from Thermodynamic Models of Minerals and Melts, IV. Adiabatic Decompression and the Composition and Mean Properties of Mid-Ocean Ridge Basalts. *Journal of Petrology* 42: 963–998.

Asimow, P. D., Dixon, J. E., and Langmuir, C. H. 2004. A Hydrous Melting and Fractionation Model for Mid-Ocean Ridge Basalts: Application to the Mid-Atlantic Ridge Near the Azores: Hydrous Melting and Fractionation. *Geochemistry, Geophysics, Geosystems* 5: Q01E16.

Asimow, P. D., and Ghiorso, M. S. 1998. Algorithmic Modifications Extending MELTS to Calculate Subsolidus Phase Relations. *American Mineralogist* 83: 1127–32.

Balta, J. B., and McSween, H. Y. 2013. Application of the MELTS Algorithm to Martian Compositions and Implications for Magma Crystallization: Applicability of MELTS to Mars. *Journal of Geophysical Research: Planets* 118: 2502–19.

Balta, J. B., Sanborn, M. E., Udry, A., Wadhwa, M., and McSween, H. Y., Jr. 2015. Petrology and Trace Element Geochemistry of Tissint, the Newest Shergottite Fall. *Meteoritics & Planetary Science* 50: 63–85.

Baratoux, D., Toplis, M. J., Monnereau, M., and Gasnault, O. 2011. Thermal History of Mars Inferred from Orbital Geochemistry of Volcanic Provinces. *Nature* 472: 338–341.

Barnes, J. J., McCubbin, F. M., Santos, A. R., Day, J. M., Boyce, J. W., Schwenzer, S. P., Ott, U., et al. 2020. Multiple Early-Formed Water Reservoirs in the Interior of Mars. *Nature Geoscience* 13: 260–64.

Bertka, C. M., and Fei, Y. 1997. Mineralogy of the Martian Interior up to Core-Mantle Boundary Pressures. *Journal of Geophysical Research: Solid Earth* 102: 5251–64.

Bertka, C. M., and Holloway, J. R. 1994a. Anhydrous Partial Melting of an Iron-Rich Mantle I: Subsolidus Phase Assemblages and Partial Melting Phase Relations at 10 to 30 kbar. *Contributions to Mineralogy and Petrology* 115: 313–322.

Bertka, C. M., and Holloway, J. R. 1994b. Anhydrous Partial Melting of an Iron-Rich Mantle II: Primary Melt Compositions at 15 kbar. *Contributions to Mineralogy and Petrology* 115: 323–338.

Blinova, A., and Herd, C. D. K. 2009. Experimental Study of Polybaric REE Partitioning Between Olivine, Pyroxene and Melt of the Yamato 980459 Composition: Insights into the Petrogenesis of Depleted Shergottites. *Geochimica et Cosmochimica Acta* 73: 3471–92.

Borg, L. E., and Draper, D. S. 2003. A Petrogenetic Model for the Origin and Compositional Variation of the Martian Basaltic Meteorites. *Meteoritics & Planetary Science* 38: 1713–31.

Bouvier, L. C., Costa, M. M., Connelly, J. N., Jensen, N. K., Wielandt, D., Storey, M., Nemchin, A. A., et al. 2018. Evidence for Extremely Rapid Magma Ocean Crystallization and Crust Formation on Mars. *Nature* 558: 586–89.

Brandon, A. D., Puchtel, I. S., Walker, R. J., Day, J. M. D., Irving, A. J., and Taylor, L. A. 2012. Evolution of the Martian Mantle Inferred from the ^{187}Re–^{187}Os Isotope and Highly Siderophile Element Abundance Systematics of Shergottite Meteorites. *Geochimica et Cosmochimica Acta* 76: 206–235.

Brandon, A. D., Walker, R. J., Morgan, J. W., and Goles, G. G. 2000. Re-Os Isotopic Evidence for Early Differentiation of the Martian Mantle. *Geochimica et Cosmochimica Acta* 64: 4083–95.

Castle, N., and Herd, C. D. 2017. Experimental Petrology of the Tissint Meteorite: Redox Estimates, Crystallization Curves, and Evaluation of Petrogenetic Models. *Meteoritics & Planetary Science* 52: 125–146.

Collinet, M., Medard, E., and Charlier, B. 2015. Melting of the Primitive Martian Mantle at 0.5–2.2 GPa and the Origin of Basalts and Alkaline Rocks on Mars. *Earth and Planetary Science Letters* 427: 83–94.

Collinet, M., Plesa, A., Grove, T. L., Schwinger, S., Ruedas, T., and Breuer, D. 2021. MAGMARS: A Melting Model for the Martian Mantle and FeO-Rich Peridotite. *Journal of Geophysical Research: Planets* 126: e2021JE006985.

Collinet, M., Plesa, A. C., Ruedas, T., Schwinger, S., and Breuer, D. 2023. The Temperature and Composition of the Mantle Sources of Martian Basalts. *Geophysical Research Letters* 50: 2023GL103537.

Connolly, J. A. D. 2009. The Geodynamic Equation of State: What and how. *Geochemistry, Geophysics, Geosystems* 10: Q10014.

Davis, F. A., Hirschmann, M. M., and Humayun, M. 2011. The Composition of the Incipient Partial Melt of Garnet Peridotite at 3 GPa and the Origin of OIB. *Earth and Planetary Science Letters* 308: 380–390.

Day, J. M. D., Tait, K. T., Udry, A., Moynier, F., Liu, Y., and Neal, C. R. 2018. Martian Magmatism from Plume Metasomatized Mantle. *Nature Communications* 9: 1–8.

Debaille, V., Yin, Q.-Z., Brandon, A. D., and Jacobsen, B. 2008. Martian Mantle Mineralogy Investigated by the ^{176}Lu–^{176}Hf and ^{147}Sm–^{143}Nd Systematics of Shergottites. *Earth and Planetary Science Letters* 269: 186–199.

Ding, S., Dasgupta, R., and Tsuno, K. 2020. The Solidus and Melt Productivity of Nominally Anhydrous Martian Mantle Constrained by New High Pressure-Temperature Experiments—Implications for Crustal Production and Mantle Source Evolution. *Journal of Geophysical Research: Planets* 125: e2019JE006078.

Draper, D. S., Xirouchakis, D., and Agee, C. B. 2003. Trace Element Partitioning Between Garnet and Chondritic Melt from 5 to 9 GPa: Implications for the Onset of the Majorite Transition in the Martian Mantle. *Physics of the Earth and Planetary Interiors* 139: 146–169.

Dreibus, G., and Wänke, H. 1985. Mars, a Volatile-Rich Planet. *Meteoritics* 20: 367–381.

Duncan, M. S., Schmerr, N. C., Bertka, C. M., and Fei, Y. 2018. Extending the Solidus for a Model Iron-Rich Martian Mantle Composition to 25 GPa. *Geophysical Research Letters* 45: 10–211.

El Maarry, M. R., Gasnault, O., Toplis, M. J., Baratoux, D., Dohm, J. M., Newsom, H. E., Boynton, W. V., and Karunatillake, S. 2009. Gamma-Ray Constraints on the Chemical Composition of the Martian Surface in the Tharsis Region: A Signature of Partial Melting of the Mantle? *Journal of Volcanology and Geothermal Research* 185: 116–122.

Elkins-Tanton, L. T. 2008. Linked Magma Ocean Solidification and Atmospheric Growth for Earth and Mars. *Earth and Planetary Science Letters* 271: 181–191.

Elkins-Tanton, L. T., Zaranek, S. E., Parmentier, E. M., and Hess, P. C. 2005. Early magnetic field and magmatic activity on Mars from magma ocean cumulate overturn. *Earth and Planetary Science Letters* 236: 1–12.

Ferdous, J., Brandon, A. D., Peslier, A. H., and Pirotte, Z. 2017. Evaluating Crustal Contributions to Enriched Shergottites from the Petrology, Trace Elements, and Rb-Sr and Sm-Nd Isotope Systematics of Northwest Africa 856. *Geochimica et Cosmochimica Acta* 211: 280–306.

Filiberto, J., and Dasgupta, R. 2011. Fe^{2+}–Mg Partitioning Between Olivine and Basaltic Melts: Applications to Genesis of Olivine-Phyric Shergottites and Conditions of Melting in the Martian Interior. *Earth and Planetary Science Letters* 304: 527–537.

Filiberto, J., and Treiman, A. H. 2009. Martian Magmas Contained Abundant Chlorine, but Little Water. *Geology* 37: 1087–90.

Foley, C. N., Wadhwa, M., Borg, L. E., Janney, P. E., Hines, R., and Grove, T. L. 2005. The Early Differentiation History of Mars from ^{182}W-^{142}Nd Isotope Systematics in the SNC Meteorites. *Geochimica et Cosmochimica Acta* 69: 4557–71.

Ghiorso, M. S., Hirschmann, M. M., Reiners, P. W., and Kress, V. C. 2002. The pMELTS: A Revision of MELTS for Improved Calculation of Phase Relations and Major Element Partitioning Related to Partial Melting of the Mantle to 3 GPa. *Geochemistry, Geophysics, Geosystems* 3: 1–35.

Ghiorso, M. S., and Sack, R. O. 1995. Chemical Mass Transfer in Magmatic Processes IV. A Revised and Internally Consistent Thermodynamic Model for the Interpolation and Extrapolation of Liquid-Solid Equilibria in Magmatic Systems at Elevated Temperatures and Pressures. *Contributions to Mineralogy and Petrology* 119: 197–212.

Ghosal, S., Sack, R. O., Ghiorso, M. S., and Lipschutz, M. E. 1998. Evidence for a Reduced, Fe-Depleted Martian Mantle Source Region of Shergottites. *Contributions to Mineralogy and Petrology* 130: 346–357.

Green, T. H., Blundy, J. D., Adam, J., and Yaxley, G. M. 2000. SIMS Determination of Trace Element Partition Coefficients Between Garnet, Clinopyroxene and Hydrous Basaltic Liquids at 2–7.5 GPa and 1080–1200°C. *Lithos* 53: 165–187.

Hauri, E. H., Wagner, T. P., and Grove, T. L. 1994. Experimental and Natural Partitioning of Th, U, Pb and Other Trace Elements Between Garnet, Clinopyroxene and Basaltic Melts. *Chemical Geology* 117: 149–166.

Herd, C. D. 2003. The oxygen fugacity of olivine-phyric Martian basalts and the components within the mantle and crust of Mars. *Meteoritics & Planetary Science* 38: 1793–1805.

Herd, C. D. K., Borg, L. E., Jones, J. H., and Papike, J. J. 2002. Oxygen Fugacity and Geochemical Variations in the Martian Basalts: Implications for Martian Basalt Petrogenesis and the Oxidation State of the Upper Mantle of Mars. *Geochimica et Cosmochimica Acta* 66: 2025–36.

Humayun, M., Nemchin, A., Zanda, B., Hewins, R. H., Grange, M., Kennedy, A., Lorand, J. P., et al. 2013. Origin and Age of the Earliest Martian Crust from Meteorite NWA 7533. *Nature* 503: 513–16.

Jacobson, S. A., and Walsh, K. J. 2015. Earth and Terrestrial Planet Formation. In *The Early Earth*, edited by J. Badro, and M. J. Walter, 49–70. Hoboken, NJ: John Wiley.

Jagoutz, E., Palme, H., Baddenhausen, H., Blum, K., Cendales, M., Dreibus, G., Spettel, B., Wänke, H., and Lorenz, V. 1979. The Abundances of Major, Minor and Trace Elements in the Earth's Mantle as Derived from Primitive Ultramafic Nodules. *10th Lunar and Planetary Science Conference*, pp. 2031–50.

Johnson, S. S., Mischna, M. A., Grove, T. L., and Zuber, M. T. 2008. Sulfur-induced greenhouse warming on early Mars. *Journal of Geophysical Research: Planets* 113(E8): E08005.

Khan, A., and Connolly, J. A. D. 2008. Constraining the Composition and Thermal State of Mars from Inversion of Geophysical Data. *Journal of Geophysical Research* 113: E07003.

Khan, A., Liebske, C., Rozel, A., Rivoldini, A., Nimmo, F., Connolly, J. A. D., Plesa, A. C., and Giardini, D. 2018. A Geophysical Perspective on the Bulk Composition of Mars. *Journal of Geophysical Research: Planets* 123: 575–611.

Kruijer, T. S., Borg, L. E., Wimpenny, J., and Sio, C. K. 2020. Onset of Magma Ocean Solidification on Mars Inferred from Mn-Cr Chronometry. *Earth and Planetary Science Letters* 542: 116315.

Langmuir, C. H., Klein, E. M., and Plank, T. 1992. Petrological Systematics of Mid-Ocean Ridge Basalts: Constraints on Melt Generation beneath Ocean Ridges. In *Mantle Flow and Melt Generation at Mid-Ocean Ridges, Geophysical. Monograph 71*, edited by J. P. Morgan, D. K. Blackmun, and J. M. Sinton, 183–280. Washington D.C: AGU.

Lapen, T. J., Righter, M., Brandon, A. D., Debaille, V., Beard, B. L., Shafer, J. T., and Peslier, A. H. 2010. A Younger Age for ALH 84001 and its Geochemical Link to Shergottite Sources in Mars. *Science* 328: 347–351.

Li, X., Zhang, C., Almeev, R. R., and Holtz, F. 2020. GeoBalance: An Excel VBA Program for Mass Balance Calculation in Geosciences. *Geochemistry* 80: 125629.

Lodders, K., and Fegley, B. 1997. An Oxygen Isotope Model for the Composition of Mars. *Icarus* 126: 373–394.

Longhi, J., Knittle, E., Holloway, J. R., and Wänke, H. 1992. The Bulk Composition, Mineralogy and Internal Structure of Mars. In *Mars*, edited by H. H. Kieffer, B. M. Jakosky, C. W. Synder, and M. S. Matthews, 184–208. Tucson, AZ: University of Arizona Press.

Matsukage, K. N., Nagayo, Y., Whitaker, M. L., Takahashi, E., and Kawasaki, T. 2013. Melting of the Martian Mantle from 1.0 to 4.5 GPa. *Journal of Mineralogical and Petrological Sciences* 108: 201–214.

McDonough, W. F., and Sun, S. S. 1995. The composition of the Earth. *Chemical Geology* 120: 223–253.

McKay, G., Wagstaff, J., and Yang, S.-R. 1986. Clinopyroxene REE Distribution Coefficients for Shergottites: The REE Content of the Shergotty Melt. *Geochimica et Cosmochimica Acta* 50: 927–937.

McSween, H. Y., Taylor, G. J., and Wyatt, M. B. 2009. Elemental Composition of the Martian Crust. *Science* 324: 736–39.

Médard, E., and Grove, T. L. 2006. Early Hydrous Melting and Degassing of the Martian Interior. *Journal of Geophysical Research* 111: E11003.

Montési, L. G. J. 2003. Clues to the Lithospheric Structure of Mars from Wrinkle Ridge Sets and Localization Instability. *Journal of Geophysical Research* 108: 5048.

Morbidelli, A., Lunine, J. I., O'Brien, D. P., Raymond, S. N., and Walsh, K. J. 2012. Building Terrestrial Planets.

Annual Review of Earth and Planetary Sciences 40: 251–275.
Morgan, J. W., and Anders, E. 1979. Chemical Composition of Mars. *Geochimica et Cosmochimica Acta* 43: 1601–10.
Morimoto, N. 1988. Nomenclature of Pyroxenes. *Mineralogy and Petrology* 39: 55–76.
Nicholls, I. A., and Harris, K. L. 1980. Experimental Rare Earth Element Partition Coefficients for Garnet, Clinopyroxene and Amphibole Coexisting with Andesitic and Basaltic Liquids. *Geochimica et Cosmochimica Acta* 44: 287–308.
Nicklas, R. W., Day, J. M., Vaci, Z., Udry, A., Liu, Y., and Tait, K. T. 2021. Uniform Oxygen Fugacity of Shergottite Mantle Sources and an Oxidized Martian Lithosphere. *Earth and Planetary Science Letters* 564: 116876.
Norman, M. D. 1999. The Composition and Thickness of the Crust of Mars Estimated from Rare Earth Elements and Neodymium-Isotopic Compositions of Martian Meteorites. *Meteoritics & Planetary Science* 34: 439–449.
Ohtani, E., and Kamaya, N. 1992. The Geochemical Model of Mars: An Estimation from the High-Pressure Experiments. *Geophysical Research Letters* 19: 2239–42.
Payré, V., and Dasgupta, R. 2022. Effects of Phosphorus on Partial Melting of the Martian Mantle and Compositions of the Martian Crust. *Geochimica et Cosmochimica Acta* 327: 229–246.
Pearson, D. G., Canil, D., and Shirey, S. B. 2003. Mantle Samples Included in Volcanic Rocks: Xenoliths and Diamonds. In *Treatise on Geochemistry*, edited by H. D. Holland, and K. K. Turekin, 171–275. Oxford: Elsevier.
Peters, T. J., Simon, J. I., Jones, J. H., Usui, T., Moriwaki, R., Economos, R. C., Schmitt, A. K., and McKeegan, K. D. 2015. Tracking the Source of the Enriched Martian Meteorites in Olivine-Hosted Melt Inclusions of Two Depleted Shergottites, Yamato 980459 and Tissint. *Earth and Planetary Science Letters* 418: 91–102.
Pommier, A., Grove, T. L., and Charlier, B. 2012. Water Storage and Early Hydrous Melting of the Martian Mantle. *Earth and Planetary Science Letters* 333: 272–281.
Prowatke, S., and Klemme, S. 2006. Trace Element Partitioning Between Apatite and Silicate Melts. *Geochimica et Cosmochimica Acta* 70: 4513–27.
Righter, K. 2017. The Lunar Meteorite Compendium. http://curator.jsc.nasa.gov/antmet/lmc/index.cfm.
Righter, K., Danielson, L. R., Pando, K., Morris, R. V., Graff, T. G., Agresti, D. G., Martin, A. M., Sutton, S. R., Newville, M., and Lanzirotti, A. 2013. Redox Systematics of Martian Magmas with Implications for Magnetite Stability. *American Mineralogist* 98: 616–628.
Righter, K., Danielson, L. R., Pando, K. M., Williams, J., Humayun, M., Hervig, R. L., and Sharp, T. G. 2015. Highly Siderophile Element (HSE) Abundances in the Mantle of Mars Are Due to Core Formation at High Pressure and Temperature. *Meteoritics & Planetary Science* 50: 604–631.
Righter, K., Rowland, R., Danielson, L. R., Humayun, M., Yang, S., Mayer, N., and Pando, K. 2020. Mantle–Melt Partitioning of the Highly Siderophile Elements: New Results and Application to Mars. *Meteoritics & Planetary Science* 55: 2741–57.
Righter, K., Yang, H., Costin, G., and Downs, R. T. 2008. Oxygen Fugacity in the Martian Mantle Controlled by Carbon: New Constraints from the Nakhlite MIL 03346. *Meteoritics & Planetary Science* 43: 1709–23.
Salters, V. J., and Longhi, J. 1999. Trace Element Partitioning During the Initial Stages of Melting beneath Mid-Ocean Ridges. *Earth and Planetary Science Letters* 166: 15–30.
Salters, V. J. M., Longhi, J. E., and Bizimis, M. 2002. Near Mantle Solidus Trace Element Partitioning at Pressures up to 3.4 GPa. *Geochemistry, Geophysics, Geosystems* 3: 1–23.
Sanloup, C., Jambon, A., and Gillet, P. 1999. A Simple Chondritic Model of Mars. *Physics of the Earth and Planetary Interiors* 112: 43–54.
Shearer, C. K., Bell, A. S., Herd, C. D., Burger, P. V., Provencio, P., Sharp, Z. D., and Papike, J. J. 2019. The Northwest Africa 8159 (NWA 8159) Martian Meteorite Part 2. Spinel-orthopyroxene intergrowths. A record of fO2 and crust-basalt interactions. *Geochimica et Cosmochimica Acta* 258: 242–257.
Smith, P. M., and Asimow, P. D. 2005. Adiabat_1ph: A new public front-end to the MELTS, pMELTS, and pHMELTS models. *Geochemistry, Geophysics, Geosystems* 6(2): Q02004.
Sobolev, A. V., Hofmann, A. W., Sobolev, S. V., and Nikogosian, I. K. 2005. An Olivine-Free Mantle Source of Hawaiian Shield Basalts. *Nature* 434: 590–97.
Stixrude, L., and Lithgow-Bertelloni, C. 2011. Thermodynamics of Mantle Minerals-II. Phase Equilibria. *Geophysical Journal International* 184: 1180–1213.
Takahashi, E. 1986. Melting of a Dry Peridotite KLB-1 up to 14 GPa: Implications on the Origin of Peridotitic Upper Mantle. *Journal of Geophysical Research: Solid Earth* 91: 9367–82.
Takahashi, E., Shimazaki, T., Tsuzaki, Y., and Yoshida, H. 1993. Melting Study of a Peridotite KLB-1 to 6.5 GPa, and the Origin of Basaltic Magmas. *Philosophical Transactions of the Royal Society of London, Series A: Physical and Engineering Sciences* 342: 105–120.
Taylor, G. J. 2013. The Bulk Composition of Mars. *Geochemistry* 73: 401–420.
Udry, A., Gazel, E., and McSween, H. Y., Jr. 2018. Formation of evolved rocks at Gale crater by crystal fractionation and implications for Mars crustal composition. *Journal of Geophysical Research: Planets* 123: 1525–40.
Udry, A., Howarth, G. H., Herd, C. D. K., Day, J. M. D., Lapen, T. J., and Filiberto, J. 2020. What Martian Meteorites Reveal about the Interior and Surface of Mars. *Journal of Geophysical Research: Planets* 125: e2020JE006523.
Usui, T., McSween, H. Y., and Floss, C. 2008. Petrogenesis of Olivine-Phyric Shergottite Yamato 980459, Revisited. *Geochimica et Cosmochimica Acta* 72: 1711–30.
van Westrenen, W., Blundy, J. D., and Wood, B. J. 2001. High Field Strength Element/Rare Earth Element Fractionation During Partial Melting in the Presence of Garnet: Implications for Identification of Mantle Heterogeneities. *Geochemistry, Geophysics, Geosystems* 2: 2000GC000133.
Wadhwa, M. 2001. Redox State of Mars' Upper Mantle and Crust from Eu Anomalies in Shergottite Pyroxene. *Science* 291: 1527–30.
Wänke, H., and Dreibus, G. 1994. Chemistry and Accretion History of Mars. *Philosophical Transactions of the Royal Society of London. Series A: Physical and Engineering Sciences* 349: 285–293.
White, D. S. M., Dalton, H. A., Kiefer, W. S., and Treiman, A. H. 2006. Experimental Petrology of the Basaltic Shergottite Yamato-980459: Implications for the Thermal

Structure of the Martian Mantle. *Meteoritics & Planetary Science* 41: 1271–90.
Wittmann, A., Korotev, R. L., Jolliff, B. L., Irving, A. J., Moser, D. E., Barker, I., and Rumble, D., III. 2015. Petrography and Composition of Martian Regolith Breccia Meteorite Northwest Africa 7475. *Meteoritics & Planetary Science* 50: 326–352.
Wu, Y., Li, Q. L., Che, X., and Liao, S. 2021. Heterogeneous Martian Mantle: Evidence from Petrology, Mineral Chemistry, and In Situ U-Pb Chronology of the Basaltic Shergottite Northwest Africa 8653. *Geochimica et Cosmochimica Acta* 309: 352–365.
Yang, S., Humayun, M., Righter, K., Jefferson, G., Fields, D., and Irving, A. J. 2015. Siderophile and Chalcophile Element Abundances in Shergottites: Implications for Martian Core Formation. *Meteoritics & Planetary Science* 50: 691–714.
Yoshizaki, T., and McDonough, W. F. 2020. The Composition of Mars. *Geochimica et Cosmochimica Acta* 273: 137–162.
Zhang, J., and Herzberg, C. 1994. Melting Experiments on Anhydrous Peridotite KLB-1 from 5.0 to 22.5 GPa. *Journal of Geophysical Research: Solid Earth* 99: 17729–42.
Zuber, M. T., Solomon, S. C., Phillips, R. J., Smith, D. E., Tyler, G. L., Aharonson, O., Balmino, G., et al. 2000. Internal Structure and Early Thermal Evolution of Mars from Mars Global Surveyor Topography and Gravity. *Science* 287: 1788–93.

SUPPORTING INFORMATION

Additional supporting information may be found in the online version of this article.

Figure S1. Plot of pMELTS calculated olivine Fo against the Mg# of model compositions of bulk Mars. Dash line is 1:1 line, and full line indicates Fo_{77} of Martian mantle olivine estimated by Filiberto and Dasgupta (2011).

Figure S2. Compositional dependence of mineral chemistry defined by pMELTS calculations: (a–c) proportions of wollastonite (Wo), enstatite (En), and ferrosilite (Fs) of mantle clinopyroxene correlate with Ca/Si ratios of BSM; and (d–f) proportions of almandine (Alm) and pyrope (Py) of mantle garnet correlate with Mg# of BSM, while that of grossular (Gro) does not.

Figure S3. The $Fe^{3+}/\sum Fe$ ratio as a function of fO_2 (ΔFMQ) constrained by MELTS. The DW94 composition was used as the starting composition. MELTS calculations were run at 1300°C and 3 GPa, with increasing $Fe^{3+}/\sum Fe$ by 0.01 interval from 0.01 to 0.07. Gray arrows show that $Fe^{3+}/\sum Fe$ at 0.02 corresponds to $\sim\Delta$FMQ-2 in terms of fO_2. The measurements of synthetic shergottites from Righter et al. (2013) are shown for comparison.

Figure S4. A compilation of the proposed trace elemental compositions of Martian primitive mantle (PM) for the five models where such data are provided.

Table S1. The composition of each mineral phase at 2, 3, 4, and 5 GPa from pMELTS calculations.

Table S2. The trace elemental partition coefficients values from experimental studies.